On the Calculation of Uncertainty Statistics with Error Bounds for CFD Calculations Containing Random Parameters and Fields

Timothy J. Barth
NASA Ames Research Center, Moffett Field, California 94035, USA

Abstract

This chapter discusses the ongoing development of combined uncertainty and error bound estimates for computational fluid dynamics (CFD) calculations subject to imposed random parameters and random fields. An objective of this work is the construction of computable error bound formulas for output uncertainty statistics that guide CFD practitioners in systematically determining how accurately CFD realizations should be approximated and how accurately uncertainty statistics should be approximated for output quantities of interest. Formal error bounds formulas for moment statistics that properly account for the presence of numerical errors in CFD calculations and numerical quadrature errors in the calculation of moment statistics have been previously presented in [8]. In this past work, hierarchical node-nested dense and sparse tensor product quadratures are used to calculate moment statistics integrals. In the present work, a framework has been developed that exploits the hierarchical structure of these quadratures in order to simplify the calculation of an estimate of the quadrature error needed in error bound formulas. When signed estimates of realization error are available, this signed error may also be used to estimate output quantity of interest probability densities as a means to assess the impact of realization error on these density estimates. Numerical results are presented for CFD problems with uncertainty to demonstrate the capabilities of this framework.

1 Introduction

Computational fluid dynamics (CFD) calculations often contain both numerical error arising from finite-dimensional approximation (e.g., grids, time steps, basis functions) and statistical uncertainty arising from the statistical characterization of model parameters and fields. Although the quantification of CFD numerical errors and the propagation of uncertainties have been individually studied in detail, the interaction of numerical realization errors within uncertainty propagation has not received sufficient attention, and is the focus of this work.

An important task in uncertainty quantification is the forward propagation of uncertainty information to determine the statistical uncertainty of output quantities of interest. This work considers the class of *non-intrusive* uncertainty quantification (UQ) methods that determine the uncertainty of output quantities of interest by performing CFD realizations for specific values of uncertain parameters and uncertain fields. Unfortunately, the accuracy of these computed statistics may be severely compromised by the presence of numerical errors of two types: (1) numerical errors occurring in

CFD realizations and (2) numerical errors occurring in the calculation of output statistics. A unified framework for combined non-intrusive uncertainty and error bound estimation has been developed in [8] such that:

- If the simulation has no uncertainty, then standard *a posteriori* error bound estimates are obtained.
- If the simulation has no numerical error, then standard uncertainty estimates are obtained.
- If the simulation has both uncertainty and numerical error, then uncertainty statistics with error bound estimates are obtained.

Particular attention is given to the calculation of expectation and variance moment statistics. For a function $f(x)$ and probability density $p(x)$, the expectation (mean) is calculated from the integral:

$$E[f] = \int f(x)\, p(x)\, dx \tag{1}$$

and the variance (standard deviation squared) is calculated from the integral:

$$V[f] = \sigma^2[f] = \int (f(x) - E[f])^2\, p(x)\, dx \tag{2}$$

In addition, often there is a keen interest in estimating the output probability density distribution denoted by p_f:

$$Pr[a \leq f \leq b] = \int_a^b p_f(x)\, dx \tag{3}$$

For many problems of interest, the function f can not be exactly evaluated and the required output statistics must be numerically approximated. Thus, error bound estimates for output statistics provide valuable information concerning the quality and reliability of computed statistics. More specifically, computable error bound estimates provide quantitative guidance when performing practical calculations with uncertainty:

- How accurate is a computed output statistic?
- How does realization error affect the accuracy of a computed output statistic?
- How does statistics integral quadrature error affect the accuracy of computed moment statistics?
- To improve the accuracy of computed output statistics, should additional resources be devoted to solving realizations more accurately or to improving the accuracy of computed statistics?

The ability to quantitatively answer these questions, together with error balancing strategies, is a powerful new capability in uncertainty quantification.

2 Background

2.1 The Non-Intrusive Forward Propagation of Uncertainty in PDE Models

The deterministic partial differential equations (PDEs) governing popular formulations of CFD often utilize models containing uncertain parameters that may be mathematically treated as random variables. This development and its impact on computed output quantities of interest is discussed next.

2.1.1 A Deterministic PDE Model

A starting point is the well-posed deterministic system of m conservation laws in d space dimensions that depends on M parameters, $\boldsymbol{\xi} \in \mathbb{R}^M$:

$$\begin{aligned} \partial_t \boldsymbol{u}(\boldsymbol{x},t;\boldsymbol{\xi}) + \sum_{i=1}^{d} \partial_{x_i} \boldsymbol{f}_i(\boldsymbol{u}(\boldsymbol{x},t;\boldsymbol{\xi});\boldsymbol{\xi}) &= 0 \\ \boldsymbol{u}(\boldsymbol{x},0;\boldsymbol{\xi}) &= \boldsymbol{u}_0(\boldsymbol{x};\boldsymbol{\xi}) \end{aligned} \tag{4}$$

with $\boldsymbol{x} \in \Omega \subset \mathbb{R}^d$ and $\boldsymbol{u}, \boldsymbol{f}_i \in \mathbb{R}^m$. The notation $u(\boldsymbol{x},t;\boldsymbol{\xi})$ has been chosen to highlight the dependence of the solution on parameters $\boldsymbol{\xi}$ in the problem. This system, together with suitable spatial boundary conditions (that may also depend on $\boldsymbol{\xi}$), is representative of many conservation law systems arising in computational science such as the equations of compressible flow utilized in CFD.

2.1.2 A Random Variable PDE Model

Let (Θ, Σ, P) denote the probability space of event outcomes, σ-algebra, and probability measure, respectively. Suppose the parameters $\boldsymbol{\xi}$ are now random variables depending on the random events $\omega \in \Theta$ that satisfy given probability laws. A random variable form of the conservation law system is now given by:

$$\begin{aligned} \partial_t \boldsymbol{u}(\boldsymbol{x},t,\omega;\boldsymbol{\xi}(\omega)) + \sum_{i=1}^{d} \partial_{x_i} \boldsymbol{f}_i(\boldsymbol{u}(\boldsymbol{x},t,\omega;\boldsymbol{\xi}(\omega)),\boldsymbol{\xi}(\omega)) &= 0 \\ \boldsymbol{u}(\boldsymbol{x},0,\omega;\boldsymbol{\xi}(\omega)) &= \boldsymbol{u}_0(\boldsymbol{x};\boldsymbol{\xi}(\omega)) \end{aligned} \tag{5}$$

The statistical behavior of $\boldsymbol{\xi}(\omega)$ is characterized here by a probability density $p_{\boldsymbol{\xi}}(\boldsymbol{\xi})$ such that $dP(\omega) = p_{\boldsymbol{\xi}}(\boldsymbol{\xi}) d\boldsymbol{\xi}(\omega)$. For simplicity, it is assumed in later examples that the random variables are independent so that the probability density is of product form:

$$p_{\boldsymbol{\xi}}(\boldsymbol{\xi}) = \prod_{i=1}^{M} p_{\xi_i}(\xi_i) \tag{6}$$

When the number of random variable parameters is large, a complete representation of the solution $\boldsymbol{u}(\boldsymbol{x},t,\omega;\boldsymbol{\xi}(\omega))$ is a high-dimensional object. Consequently, finding the solution to this problem either analytically or numerically can be cost prohibitive.

2.2 Output Quantities of Interest

For many practical problems, rather than explicitly representing the entire random variable solution, $\boldsymbol{u}(\boldsymbol{x},t,\omega;\boldsymbol{\xi}(\omega))$, there is often interest in quantifying uncertainty statistics of solution-derived output quantities of interest (QOI) denoted here by $J[u(\boldsymbol{x},t,\omega;\boldsymbol{\xi}(\omega))]$. Output QOIs may include random variable functionals, graphs, and fields. Recall that in forward uncertainty propagation, the probability laws associated with random variable parameters $\boldsymbol{\xi}$ are *given* and the primary task at hand is to characterize the probability law associated with output quantities of interest, $J[u(\boldsymbol{x},t,\omega;\boldsymbol{\xi}(\omega))]$. This probability law may be characterized either:

- Incompletely by the calculation of moment statistics such as expectation and variance for the QOI.
- Completely by the calculation of the probability density function for the QOI.

For problems with many sources of uncertainty, $J[u(\boldsymbol{x},t,\omega;\boldsymbol{\xi}(\omega))]$ is still a high-dimensional object so the estimation of these probability law characterizations is cost prohibitive. Rather than directly constructing high-dimensional random variable representations of the output quantities of interest, non-intrusive uncertainty propagation methods calculate a finite set of N decoupled deterministic numerical realizations of the PDE model, $u_h(\boldsymbol{x},t;\boldsymbol{\xi})$, for distinct parameter values:

$$\{\boldsymbol{\xi}^{(1)},\ldots,\boldsymbol{\xi}^{(N)}\} \tag{7}$$

yielding solution realizations

$$\{u_h(\boldsymbol{x},t;\boldsymbol{\xi}^{(1)}),\ldots,u_h(\boldsymbol{x},t;\boldsymbol{\xi}^{(N)})\} \tag{8}$$

and output quantities of interest from realizations

$$\{J[u_h(\boldsymbol{x},t;\boldsymbol{\xi}^{(1)})],\ldots,J[u_h(\boldsymbol{x},t;\boldsymbol{\xi}^{(N)})]\} \tag{9}$$

For the uncertainty propagation methods considered here, the values $\boldsymbol{\xi}^{(i)}$ are chosen as follows:

- At quadrature points when moment statistics of the QOI are sought, see Section 2.3.
- At interpolation points forming a response surface when a QOI probability density approximation is sought, see Section 5.

This approach is referred to as "non-intrusive" uncertainty propagation since it does not require modifications to an existing numerical method for calculating realizations other than the ability to change parameter values for each realization.

2.3 Numerical Quadratures for Moment Statistics

Let $I[f]$ denote a definite integral in d dimensions:

$$I[f] = \int_{[0,1]^d} f(x)\,dx \tag{10}$$

Recall that statistics integrals such as expectation and variance may be transformed to this form when the probability density function is an independent (separable) product form in d dimensions:

$$p(y) = p_{y_1}(y_1)p_{y_2}(y_2)\cdots p_{y_d}(y_d)$$

In this case, a transformed vector variable x can be found such that $dx = p(y)dy$, using the cumulative probability distribution function associated with each p_{y_i} for $i = 1,\ldots,d$. This permits a transformation of the integral to the unit cube, i.e.:

$$I[f] = \int_D f(y)\,p(y)\,dy = \int_{[0,1]^d} f(y(x))\,dx \tag{11}$$

Let $Q_N[f]$ denote an N-point numerical quadrature approximation to $I[f]$ with weights w_i and evaluation points $\boldsymbol{\xi}^{(i)}$:

$$Q_N[f] = \sum_{i=1}^{N} w_i f(\boldsymbol{\xi}^{(i)}) \tag{12}$$

with numerical quadrature error denoted by $R_N[f]$, i.e.:

$$R_N[f] = I[f] - Q_N[f] \tag{13}$$

Efficient quadratures $Q_N[\cdot]$ are considered in Section 2.5 that also provide straightforward estimates of the quadrature error $R_N[\cdot]$. These quadratures with quadrature error estimates are necessary ingredients in error bound formulas for moment statistics.

2.4 A Survey of Quadrature Methods

Several candidate methods exist for numerical quadrature of the integral (10). The locations of integrand evaluation for these methods are depicted in Figure 1 and quadrature error properties are

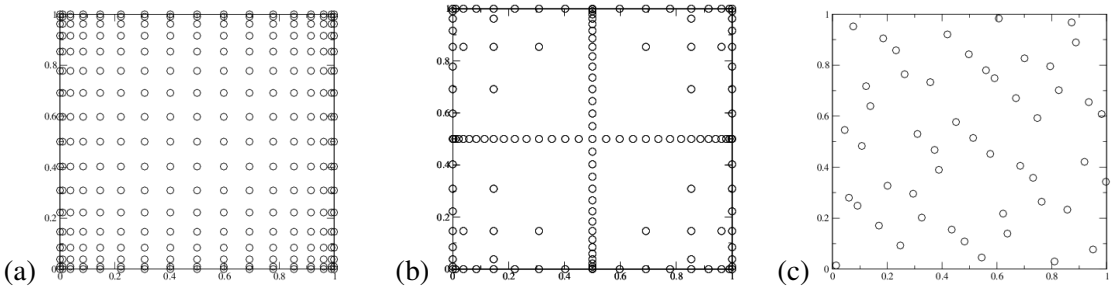

Figure 1. Quadrature point locations for (a) dense tensor product, (b) sparse tensor product, and (c) random sampling.

summarized in Table 1. For a small number of dimensions, dense tensor product methods based on global approximation are often used. More specifically, efficient dense tensor product quadrature evaluation based on the hierarchical node-nested Clenshaw-Curtis [14] and Gauss-Patterson [29]

Table 1. Summary of d-dimensional quadrature methods utilizing N evaluations.

Quadrature Method	Quadrature Error	Requirements
Global Dense Tensor Product	$\mathscr{O}(N^{-r/d})$	r bounded derivatives
Global Sparse Tensor Product	$\mathscr{O}(N^{-r}(\log N)^{(d-1)(r+1)})$	r bounded mixed derivatives
Piecewise Polynomial Tensor Product	$\mathscr{O}(N^{-(p+1)/d})$	p order local polynomials
Monte Carlo Sampling	$\mathscr{O}(N^{-1/2})$	bounded variance
Quasi-Monte Carlo Sampling	$\mathscr{O}(N^{-1}(\log N)^d)$	bounded variance

formulas are particularly useful in the present work because these quadratures also provide computable quadrature error estimates at little added cost. These quadratures are discussed in detail in Section 2.5. As the number of dimensions increases, dense tensor product quadratures become prohibitively expensive, and so sparse tensor product quadratures based on Smolyak [38] sparse grids are often then used instead. These sparse tensor product quadratures may also utilize Clenshaw-Curtis and Gauss-Patterson quadratures [27, 18] and thus retain the hierarchical node-nested structure needed for quadrature error estimates. As the number of dimensions increases further, sampling methods based on Monte Carlo random sampling [25] and low discrepancy quasi-random sampling [26] are preferred. Methods such as Monte Carlo random sampling have a well-known computable quadrature error estimate, $R_N[f] = \sqrt{V[f]/N}$. Thus, the error bound formulas described here apply without major modification to these methods as well. We now consider dense and sparse product quadratures and defer a discussion of the sampling methods to a separate work.

2.5 Hierarchical Node-Nested Quadratures with Quadrature Error Estimates

Hierarchical node-nested quadratures permit the efficient approximation of integrals while also providing a quadrature error estimate.

Let L denote a numbering of levels, N_L the number of univariate quadrature evaluation points at level L with $N_L < N_{L'}$ if $L < L'$, and $Q_L^{(1)}[\cdot]$ a quadrature at level L, i.e.:

$$Q_L^{(1)}[f] \equiv \sum_{i=1}^{N_L} w_i^{(j)} f(x_i^{(j)})$$

Of particular interest are hierarchical multi-level quadratures that satisfy the following:

$$\lim_{L\to\infty} \sup \left(N_L^r \| I^{(1)}[f] - Q_L^{(1)}[f] \| \right) < \infty \ , \quad \forall r \in \mathbb{N} \tag{14}$$

whenever f possesses r bounded derivatives. Satisfaction of (14) implies the quadrature error estimate for level L:

$$\| I^{(1)}[f] - Q_L^{(1)}[f] \| = \mathscr{O}(N_L^{-r}) \tag{15}$$

Brass [13] has shown that multi-level positive-weighted quadrature formulas that are exact for polynomials of degree strictly less than N_L satisfy Eq. (14) and the quadrature error estimate Eq. (15). Two particular multi-level quadrature formulas that satisfy these requirements are the Clenshaw-Curtis [14] quadrature formula and the Gauss-Patterson [29] quadrature formula. The node-nested

hierarchy in these two methods makes them very efficient; i.e., all quadrature evaluation points in level L are contained in level $L+1$. Evaluation points for these quadrature formulas are shown in Figure 2. Level L of the Clenshaw-Curtis quadrature requires $2^{L-1}+1$ evaluations and integrates

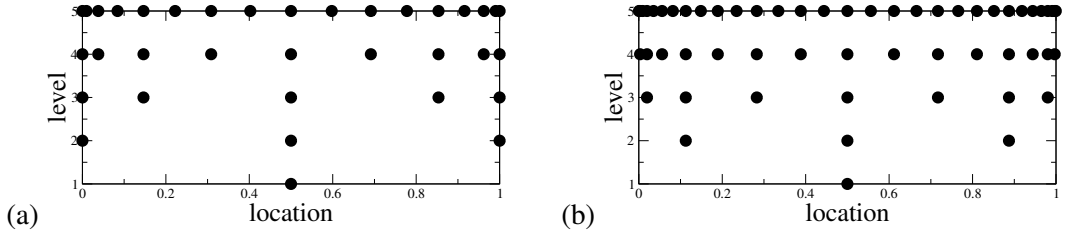

Figure 2. Node-nested quadratures point locations: (a) Clenshaw-Curtis quadrature with $N_{level} = 2^{(level-1)} + 1$, and (b) Gauss-Patterson with $N_{level} = 2^{level} - 1$ for $level > 1$ and $N_1 = 1$.

2^{L-1} polynomials exactly for $L \geq 2$. Level L of the Gauss-Patterson quadrature requires $2^L - 1$ evaluations for $L > 1$ and integrates $3 \cdot 2^{L-1} - 1$ degree polynomials exactly for $L \geq 2$. Because both quadratures satisfy the Brass conditions, they have a quadrature error estimate given by:

$$\|I^{(1)}[f] - Q_L^{(1)}[f]\| = \mathscr{O}(2^{-rL}) \tag{16}$$

2.5.1 Dense Tensor Product Clenshaw-Curtis and Gauss-Patterson Quadrature with Quadrature Error Estimate

Dense tensor product quadrature takes the form:

$$\begin{aligned} Q_L^{(d)}[f] &\equiv \left(Q_{L_1}^{(1)} \otimes \cdots \otimes Q_{L_d}^{(1)}\right)[f] \\ &= \sum_{i_1=1}^{N_{L_1}} \cdots \sum_{i_d=1}^{N_{L_d}} w_{i_1}^{(L_1)} \cdot w_{i_d}^{(L_d)} f(\boldsymbol{x}_1, \ldots, \boldsymbol{x}_d) \end{aligned} \tag{17}$$

with the total number of evaluations given by $N = \prod_{j=1}^{d} N_{L_j}$. When $Q_{L_j}^{(1)}$ corresponds to either the univariate Clenshaw-Curtis or the univariate Gauss-Patterson quadrature and $L_1 = L_2 = \cdots = L_d = L$, then the total number of evaluations is $\mathscr{O}(2^{dL})$ and the quadrature error reduces to (see for example [37]):

$$|I^{(d)}[f] - Q_L^{(d)}[f]| = \mathscr{O}(N^{-r/d}) = \mathscr{O}(2^{-rL})$$

Assuming that the unknown leading $\mathscr{O}(\cdot)$ constant does not oscillate when L is varied and remains approximately constant even for modest values of L, the following computable quadrature error formula is readily obtained:

$$R_L^{(d)}[f] \equiv I^{(d)}[f] - Q_L^{(d)}[f] \approx \frac{1}{2^r - 1}(Q_L^{(d)}[f] - Q_{L-1}^{(d)}[f]) \tag{18}$$

with

$$2^r = \frac{Q_{L-1}^{(d)}[f] - Q_{L-2}^{(d)}[f]}{Q_L^{(d)}[f] - Q_{L-1}^{(d)}[f]} \tag{19}$$

Although this is a parameter-free three-level quadrature error estimate, the performance of (19) can be unreliable when the underlying data lacks regularity. For this reason, lower and upper bounds on the smoothness parameter r are enforced, i.e., r is constrained to an interval:

$$r_{min} \leq r \leq r_{max} \tag{20}$$

with values $r_{min} = 1$ and $r_{max} = 6$ used in practical applications. Observe that if $r_{min} = r_{max}$, then the quadrature estimate (18) only depends on the two finest levels and the coarsest level is not used in the quadrature error estimate.

2.5.2 Sparse Tensor Product Clenshaw-Curtis and Gauss-Patterson Quadrature with Quadrature Error Estimate

Unfortunately, dense tensor product quadratures grow exponentially in complexity with respect to the number of dimensions. A quadrature of just two points in d dimensions requires:

$$N^{dense} = \mathscr{O}(2^d) \qquad \text{(dense product quadratures)} \tag{21}$$

evaluations. In contrast, complete polynomials of degree P in d dimensions require only the following number of evaluations:

$$N^{poly} = \binom{P+d}{d} \approx \frac{d^P}{P!} \qquad \text{(complete polynomials)} \tag{22}$$

This large gap indicates that dense product quadratures contain many unneeded evaluations. The sparse tensor product quadrature of Smolyak [38] offers a dramatic reduction in the number of evaluations required for a given precision P and dimension d when compared to dense product quadrature.

Sparse tensor product formulas are compactly written in terms of a multi-index, $\boldsymbol{i} \in \mathbb{N}^d$, so that a given product rule may be written as $Q^{(1)}_{N_{L_1}} \otimes \cdots \otimes Q^{(1)}_{N_{L_d}}$ with product level $|\boldsymbol{i}| = \sum_{j=1}^d i_j$. Using this compact notation, Smolyak sparse grid quadratures with maximum level L in d dimensions have the form:

$$Q^{(d)}_L[f] = \sum_{L-d+1 \leq |\boldsymbol{i}| \leq L} (-1)^{L-|\boldsymbol{i}|} \binom{d-1}{L-|\boldsymbol{i}|} (Q^{(1)}_{N_{L_1}} \otimes \cdots \otimes Q^{(1)}_{N_{L_d}})[f] \tag{23}$$

Novak and Ritter [27] have analyzed sparse tensor product quadratures using hierarchical multi-level Clenshaw-Curtis and Gauss-Patterson formulas. Sparse grid quadratures attain a polynomial precision P equal to $2L+1$ and require $\mathscr{O}\left(\frac{(2d)^P}{P!}\right)$ evaluations. Table 2 gives the number of quadrature evaluations required for sparse and dense forms of Clenshaw-Curtis and Gauss-Patterson quadrature for dimensions $d = 4$ and $d = 8$ and levels $L = 2,3,4,5$. The sparse tensor product Clenshaw-Curtis quadrature is a vast improvement in complexity over the dense product counterpart and differs from the use of complete polynomials by a factor 2^P.

The task of finding a computable quadrature estimate begins with a quadrature error estimate given by Wasilkowski and Woźniakowski [42] for $L \geq d$:

$$|I^{(d)}[f] - Q^{(d)}_L[f]| = \mathscr{O}(L^{(d-1)(r+1)} 2^{-rL}) \tag{24}$$

Table 2. Number of evaluations required for dense and sparse forms of Clenshaw-Curtis (CC) and Gauss-Patterson (GP) quadrature for dimensions $d = 4$ and $d = 8$ at levels $L = 2,3,4,5$.

L	Dense d=4 N(CC)	Dense d=4 N(GP)	Sparse d=4 N(CC)	Sparse d=4 N(GP)	Dense d=8 N(CC)	Dense d=8 N(GP)	Sparse d=8 N(CC)	Sparse d=8 N(GP)
2	81	81	9	9	6561	6561	17	17
3	625	2401	41	49	390625	5764801	145	161
4	6561	50625	137	209	$\mathscr{O}(10^8)$	$\mathscr{O}(10^{10})$	849	1121
5	83521	923521	401	769	$\mathscr{O}(10^{10})$	$\mathscr{O}(10^{12})$	3937	6401

Again assuming that the unknown leading $\mathscr{O}(\cdot)$ constant does not oscillate in sign when L is varied and remains approximately constant even for modest values of $L \geq d$, the following computable quadrature error estimate is readily obtained:

$$R_L^{(d)}[f] \equiv I^{(d)}[f] - Q_L^{(d)}[f] \approx \frac{1}{\left(\frac{L-1}{L}\right)^{(d-1)(r+1)} 2^r - 1} (Q_L^{(d)}[f] - Q_{L-1}^{(d)}[f]) \tag{25}$$

where r is calculated from the given parameters d and L by solving:

$$\frac{Q_{L-1}^{(d)}[f] - Q_{L-2}^{(d)}[f]}{Q_L^{(d)}[f] - Q_{L-1}^{(d)}[f]} = \frac{2^{2r} g(r;L-2,d) - 2^r g(r;L-1,d)}{2^r g(r;L-1,d) - g(r;L,d)} \tag{26}$$

with $g(r;L,d) \equiv L^{(d-1)(r+1)}$. Equation (25) reveals a strong dependence on the smoothness parameter r. In sharp contrast to the dense tensor products, the right-hand-side denominator term of the sparse error estimate may not be positive (or bounded) when the smoothness parameter r is too small for certain values of L and d. For example, when $L = 5$ and $d = 3$, then r must be greater than 1.81 for the denominator to be positive. Following the same strategy taken for the dense tensor product quadrature error estimate, the smoothness parameter r is constrained to an interval:

$$r_{min} \leq r \leq r_{max} \tag{27}$$

Depending on L and d, the lower bound may need to be larger than that used in the dense tensor product case. Note that for sparse tensor product quadrature calculations presented in Section 6.2 that correspond to $L = 4$ and $d = 2$, the formula (25) is well defined for all $r > 0.7$, so a value of $r_{min} = 1$ has been imposed.

2.5.3 Hybrid Quadrature (HYGAP) Using Piecewise Polynomial and Clenshaw-Curtis Quadrature

Hierarchical multi-level global quadratures such as Clenshaw-Curtis and Gauss-Patterson quadrature in dense tensor product form have $\mathscr{O}(2^{-rL})$ accuracy using L levels. The accuracy depends fundamentally on smooth integrands with r bounded derivatives. Sparse tensor product quadratures with $\mathscr{O}(L^{(d-1)(r+1)}2^{-rL})$ accuracy are even more demanding in requiring integrands with r bounded mixed derivatives. Unfortunately, output quantities of interest for hyperbolic problems may not have a smooth dependence on random parameters. Instead, one frequently encounters statistics

integrands that are *piecewise smooth* with a finite number of discontinuities in random variable dimensions. This observation motivated the construction of a new hybrid algorithm [7, 8] tailored for piecewise smooth integrand data. The basic idea behind the Hybrid Global Adaptive Polynomial (HYGAP) algorithm is relatively straightforward. Construct statistics quadratures in multiple dimensions using hierarchical multi-level Clenshaw-Curtis or Gauss-Patterson dense tensor products. Then for each dimension, examine integrand data to determine smoothness. When the integrand data is smooth in a dimension, use hierarchical multi-level Clenshaw-Curtis or Gauss-Patterson quadrature. When the integrand data is not smooth, construct a piecewise cubic polynomial interpolant in that dimension using data at the Clenshaw-Curtis or Gauss-Patterson points and integrate it using piecewise quadrature.

HYGAP(L)[8] Algorithm:

Step 1. Calculate quadrature point locations of an L-level Clenshaw-Curtis or Gauss-Patterson global quadrature.

Step 2. Evaluate output quantities of interest for those quadrature point values.

Step 3. Determine the smoothness of data in each dimension by estimating a one-dimensional Sobolev semi-norm measure using one-dimensional WENO piecewise polynomial approximations; see Jiang and Shu [22].

Step 4a. (smooth data) If the integrand data is smooth in a given dimension, then compute the moment statistics in that dimension using a conventional Clenshaw-Curtis or Gauss-Patterson quadrature formula.

Step 4b. (non-smooth data) If the integrand data is not smooth in a given dimension, then interpolate the integrand data at quadrature point locations using adaptive stencil piecewise polynomials. Further improve the piecewise polynomial approximation by applying a subscale resolution model [8]. Compute moment statistics by integrating the interpolated integrand data using a local piecewise quadrature.

Step 5. Compute the multi-dimensional quadrature using dense tensor products.

To demonstrate the dramatic improvement using HYGAP approximation, in [8] a random variable form of Burgers' equation with uncertain initial data was considered:

$$\frac{\partial}{\partial t}u(x,t,\omega)+\frac{\partial}{\partial x}(u^2(x,t,\omega)/2)=0 \tag{28}$$

with sinusoidal initial data with phase uncertainty:

$$u(x,0,\omega)=\sin(2\pi(x+g(\xi(\omega)))) \tag{29}$$

for $g:\mathbb{R}\mapsto\mathbb{R}$ a smooth function and $\xi(\omega)$ a random variable. The exact solution to this problem is readily constructed. At some later time, a discontinuity forms for each value of $\xi(\omega)$ so the global solution has a discontinuity that traverses obliquely through both physical and random variable dimensions as illustrated in Figure 3. The presence of discontinuities in random variable dimensions has enormous consequences in the performance of many classical techniques in UQ

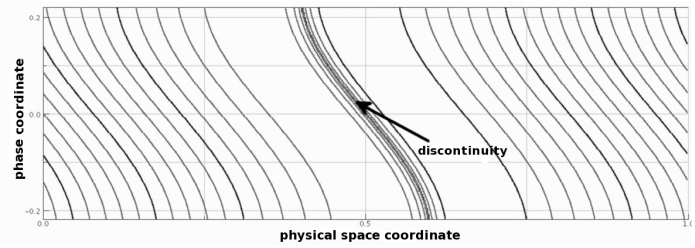

Figure 3. Solution contours for the Burgers' equation problem with phase uncertain sinusoidal initial data at time $t = .35$ with $g(\xi) = \frac{1}{10}\sin(2\pi\xi)$.

using dense and sparse tensor product quadrature. Figure 4 shows solution statistics for this Burgers' equation problem with imposed phase uncertainty satisfying a uniform probability density law, Uniform $[-.25, .25]$, with statistics approximated using Clenshaw-Curtis global quadrature. Note that similar results are obtained using a standard stochastic collocation method [39, 2]. The spuri-

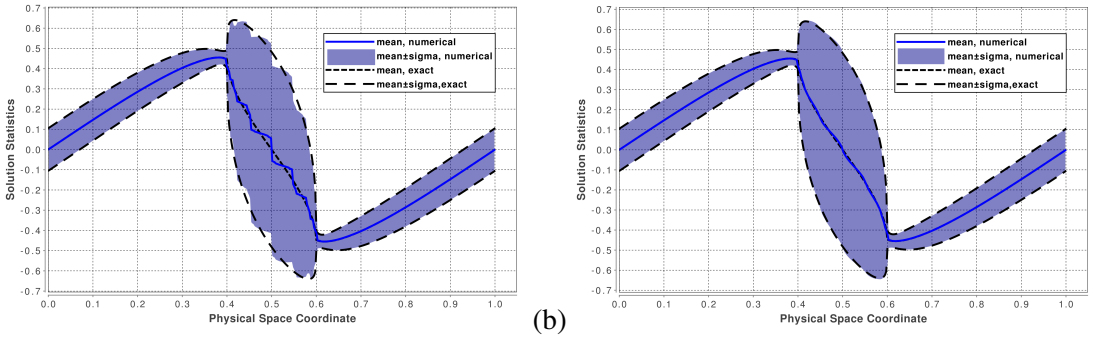

Figure 4. Expectation and standard deviation envelopes approximated from nine realizations using (a) stochastic collocation and (b) Clenshaw-Curtis HGAP approximation for the Burgers' equation problem (28) with phase uncertain initial data (29) at time $t = .35$.

ous oscillations are a result of using a global quadrature that spans a piecewise smooth integrand.

For smooth integrand data in all dimensions, applying the HYGAP algorithm at three successive levels L, $L-1$, and $L-2$ is sufficient to estimate the quadrature error using Eq. (18). When the integrand data is not smooth, the task of estimating quadrature error is difficult and not likely to be very sharp. A practical strategy is to assume a quadrature error formula of the form of Eq. (18) and then *prescribe* the value of smoothness parameter r. Keep in mind that when statistics are calculated at many spatial-temporal locations, the number of locations where r is prescribed in this way may be relatively small. In calculations shown here, $r = 1$ has been used for non-smooth integrands in the HYGAP method and satisfactory results were obtained.

2.6 Estimating Eealization Error in CFD Calculations

The error bound formulas for output moment statistics developed later in Section 3 require an estimate of the realization error:

$$\varepsilon_h \equiv J[u(\boldsymbol{x},t;\boldsymbol{\xi})] - J[u_h(\boldsymbol{x},t;\boldsymbol{\xi})] \tag{30}$$

for output quantities of interest. There are a wide variety of techniques for estimating this realization error. These include: extrapolation techniques such as Richardson's extrapolation [32] and Aitken's extrapolation [1]; patch postprocessing techniques [43, 16] that exploit superconvergence behavior of solutions; and error representation of functionals via dual problems [12, 17, 30, 23, 9, 10], among others. The numerical results of Section 6 utilize the Aitken extrapolation method or the error representation via dual problem method so these algorithms are briefly discussed.

2.6.1 Richardson and Aitken Extrapolations

Both the Richardson and Aitken extrapolation methods are sequence extrapolation/acceleration algorithms. Given a multi-level mesh hierarchy $\{\boldsymbol{u}_h, \boldsymbol{u}_{2h}, \boldsymbol{u}_{4h}, \dots\}$ where h denotes a mesh spacing parameter, assume that the output realization QOI has polynomial convergence properties that depend on the parameter h and a rate q, i.e.:

$$J(\boldsymbol{u}) - J(\boldsymbol{u}_h) = C\,h^q + \text{higher order terms} \tag{31}$$

for a constant C that does not depend on h or q. Evaluating this formula at three levels permits the elimination of the unknown constant C and the rate q, i.e.:

$$J(\boldsymbol{u}) - J(\boldsymbol{u}_h) \approx \frac{1}{2^q - 1}(J(\boldsymbol{u}_h - J(\boldsymbol{u}_{2h})) \tag{32}$$

Depending on how q is determined, the Aitken and Richardson extrapolation formulas can be obtained.

- If q is computed from
$$2^q = \frac{J(\boldsymbol{u}_{2h}) - J(\boldsymbol{u}_{4h})}{J(\boldsymbol{u}_h) - J(\boldsymbol{u}_{2h})} \tag{33}$$
then the extrapolation is referred to as Aitken's extrapolation [1] (although Aitken's extrapolation is often not written this way).
- If q is specified *a priori*, then the extrapolation is referred to as Richardson's extrapolation [32] and the extrapolation formula only uses 2 levels.

Equation (33) can be unreliable when the mesh sequence is not sufficiently resolved. Consequently, software implementations may impose lower and upper bounds on q:

$$q_{min} \le q \le q_{max} \tag{34}$$

Results presented in Section 6 have used $q_{min} = 1$ and $q_{max} = 6$ in realization QOI error estimates obtained using Aitken's extrapolation.

2.6.2 A Posteriori Error Estimation of Functionals Via Dual Problem

When an output quantity of interest $J(\boldsymbol{u}_h(\cdot;\boldsymbol{\xi});\boldsymbol{\xi})$ is a functional, the task of estimating the finite-dimensional approximation error is greatly simplified using the *a posteriori* error estimation theory developed by Eriksson *et al.* [17] and Becker and Rannacher [12]. This theory has been applied to finite-element methods [12, 17, 30, 23, 20] as well as Godunov finite-volume methods [10, 6].

The abstract *a posteriori* error estimation theory for Galerkin approximations of the model PDE in Eq. (4) consists of the following steps:

1. Solve the primal numerical problem using finite-dimensional approximation spaces $\mathscr{V}^h$. In the abstract formulation, $F(\boldsymbol{v}_h) : \mathscr{V}^h \mapsto \mathbb{R}^m$ is a forcing term (equal to zero in the present calculations) with boundary conditions assumed here to be enforced weakly via fluxes.

   Primal numerical problem: Find $\boldsymbol{v}_h \in \mathscr{V}^h$ such that:

   $$B(\boldsymbol{v}_h, \boldsymbol{w}_h) = F(\boldsymbol{w}_h) \quad , \quad \forall\, \boldsymbol{w}_h \in \mathscr{V}^h$$

2. Solve the mean-value linearized auxiliary dual problem $\overline{B}(\cdot,\cdot)$ using infinite-dimensional spaces $\mathscr{V}$ given a mean-value linearized functional $\overline{J}$.

   Linearized auxiliary dual problem: Find $\Phi \in \mathscr{V}$ such that:

   $$\overline{B}(\boldsymbol{w}, \Phi) = \overline{J}(\boldsymbol{w}) \quad , \quad \forall\, \boldsymbol{w} \in \mathscr{V}$$

3. Compute the error in a functional using the error representation formula.

   Error representation: Let π_h denote any projection into the Galerkin test space (e.g., L_2 projection, interpolation), the functional error is given by:

   $$J(\boldsymbol{u}) - J(\boldsymbol{u}_h) = F(\Phi - \pi_h\Phi) - B(\boldsymbol{u}_h, \Phi - \pi_h\Phi) \tag{35}$$

The mean-value linearization given by the error estimation theory requires knowledge of the infinite-dimensional primal solution. In addition, solutions of the dual problem are posed in infinite-dimensional spaces. These solutions are generally not available and so must be approximated. In the present computations, the mean-value linearization has been replaced by the Jacobian (tangent) linearization at the numerical solution state and the dual problem has been solved numerically using an approximation space that is one polynomial degree higher than the approximation space of the primal numerical problem. This permits the right-hand-side of Eq. (35) to be estimated.

The error representation formula (35) may be used to estimate the functional error. However, if the estimated error is too large, the formula does not provide information about how the mesh or approximation space should be modified to further reduce the error. Element-wise decomposition of the error representation formula provides a pathway for deriving element refinement indicators and a systematic means for reducing the error by refining the elements. To simplify the notation, let $Q^n = K \times I^n$ denote a space-time slab prism for a time interval, $I^n = [t^n, t^{n+1}]$. Observe that

without further approximation, the error representation formula can be written as a sum over spatial elements and N_T time intervals:

$$|J(\boldsymbol{u}) - J(\boldsymbol{u}_h)| = \left| \sum_{n=0}^{N_T-1} \sum_{Q^n} F_{Q^n}(\Phi - \pi_h\Phi) - B_{Q^n}(\boldsymbol{v}_h, \Phi - \pi_h\Phi) \right| \tag{36}$$

where $B_{Q^n}(\cdot,\cdot)$ and $F_{Q^n}(\cdot)$ are the restriction of $B(\cdot,\cdot)$ and $F(\cdot)$ to a single space-time element. Application of the generalized triangle inequality provides a localized estimate of the contribution of each space-time element to the total error in the functional:

$$|J(\boldsymbol{u}) - J(\boldsymbol{u}_h)| \leq \sum_{n=0}^{N_T-1} \sum_{Q^n} \underbrace{|F_{Q^n}(\Phi - \pi_h\Phi) - B_{Q^n}(\boldsymbol{v}_h, \Phi - \pi_h\Phi)|}_{\text{refinement indicator, } \eta(Q^n)} \tag{37}$$

These localized estimates serve as *refinement indicators* for mesh adaptivity. A commonly used strategy in mesh adaptivity, which is adopted here, is to refine a fixed fraction of element indicators $\eta(Q^n)$ that are too large and then coarsen a fixed fraction of element indicators that are too small.

3 Combined Uncertainty and Error Estimates

Recall from Section 2.2 that non-intrusive uncertainty propagation methods compute a finite number of realization output quantities of interest (QOI) for specific parameter values:

$$\{J_h^{(1)}, J_h^{(2)}, \cdots, J_h^{(N)}\} \tag{38}$$

In this formula, we have adopted the shorthand notation, $J_h^{(i)} \equiv J[u_h(\boldsymbol{x},t;\boldsymbol{\xi}^{(i)})]$. The output QOIs are calculated using a numerical method so they are finite-dimensional approximations of the exact output QOIs:

$$\{J^{(1)}, J^{(2)}, \cdots, J^{(N)}\} \tag{39}$$

where $J^{(i)} \equiv J[u(\boldsymbol{x},t;\boldsymbol{\xi}^{(i)})]$. For each realization QOI, we can assign a realization error:

$$\varepsilon_h^{(i)} \equiv J^{(i)} - J_h^{(i)} \tag{40}$$

Methods for estimating $\varepsilon_h^{(i)}$ are given in Section 2.6.

Next, recall from Section 2.3 that evaluation of moment statistics can be efficiently performed using hierarchical multi-level quadratures in dense and sparse tensor product form. For example, when applied to output QOIs, the expectation is given by:

$$E[J_h] = Q_L E[J_h] + R_L E[J_h] \tag{41}$$

with quadrature of the form

$$Q_L E[J_h] = \sum_{i=1}^{N_L} w_i J_h^{(i)} \tag{42}$$

and quadrature error $R_L E[J(\boldsymbol{u}_h(\boldsymbol{x},t;\boldsymbol{\xi}))]$ estimated from Eq. (18) for dense tensor product quadratures and Eq. (25) for sparse tensor product quadratures.

The ability to estimate quadrature errors and realization errors provides the components needed to construct error bound estimates for moment statistics.

3.1 Error Estimates for Moment Statistics Given Signed Realization and Quadrature Errors

Given the realization QOI error ε_h, a quadrature $Q_L E[\cdot]$, and quadrature error $R_L E[\cdot]$, the error in expectation can be calculated from the following formula:

$$E[J] - Q_L E[J_h] = Q_L E[\varepsilon_h] + R_L E[\varepsilon_h] + R_L E[J_h] \tag{43}$$

This formula expresses the difference between the exact expectation of the exact solution and a numerically approximated expectation of the approximated realization. This formula is purely motivational. In a realistic setting, the realization error may only be approximately known, as denoted by $\tilde{\varepsilon}_h$. Let $\tilde{J} \equiv J_h + \tilde{\varepsilon}_h$, the expectation and variance error can be estimated as follows:

• Expectation error estimate (Type I):

$$\begin{aligned} E[J] - Q_L E[J_h] &\approx E[\tilde{J}] - Q_L E[J_h] \\ &= Q_L E[\tilde{J}] + R_L E[\tilde{J}] - Q_L E[J_h] \end{aligned} \tag{44}$$

• Variance error estimate (Type I):

$$\begin{aligned} V[J] - Q_L V[J_h] &\approx E[\tilde{J}^2] - (E[\tilde{J}])^2 - (Q_L E[J_h^2] - (Q_L E[J_h])^2) \\ &= Q_L E[\tilde{J}^2] + R_L E[\tilde{J}^2] - (Q_L E[\tilde{J}] + R_L E[\tilde{J}])^2 - (Q_L E[J_h^2] - Q_L^2 E[J_h]) \end{aligned} \tag{45}$$

with equality in both formulas if $\tilde{\varepsilon}_h = \varepsilon_h$. In deriving the variance error, we have used the identity $V[J] = E[J^2] - E^2[J]$ and $Q_L V[J] = Q_L E[J^2] - Q_L E^2[J]$. Note that this latter identity does not strictly hold with equality if the quadrature weights depend on the integrand data, as in the HYGAP approximation.

3.2 Error Bound Estimates for Moment Statistics Given Realization and Quadrature Error Magnitudes

Error bound formulas for expectation and variance are derived in [8] assuming that only magnitudes of the quadrature error, $|R_N E[\cdot]|$, and magnitudes of the realization error, $|\varepsilon_h|$, are available. This situation arises often in practice. For example, the quadrature error estimate for Monte Carlo sampling given by:

$$|R_N E[J_h]| \approx \sqrt{V[J_h]/N} \tag{46}$$

only provides the magnitude of the quadrature error. As another example, the error estimate of Eriksson *et al.* [17] for functional output QOIs only estimates the magnitude. This estimate (which avoids the explicit calculation of a dual (adjoint) problem) is:

$$|\varepsilon_h| \equiv |J(u) - J(u_h)| \leq C_{int} C_{stab} \|h^s r_h\|, \quad s > 0 \tag{47}$$

where r_h is the discretization residual, C_{int} and C_{stab} are interpolation and stability constants, and h is the mesh spacing.

Assuming that only QOI realization error and quadrature error magnitudes are known, the following error bound formulas are given in [8] for expectation and variance:

• Expectation error bound (Type II):

$$\begin{aligned} |E[J(\boldsymbol{u})] - Q_L E[J(\boldsymbol{u}_h)]| &= |Q_L E[\boldsymbol{\varepsilon}_h]| + R_L E[\boldsymbol{\varepsilon}_h] + R_L E[J(\boldsymbol{u}_h)]| \\ &\leq |Q_L E[|\boldsymbol{\varepsilon}_h|]| + |R_L E[|\boldsymbol{\varepsilon}_h|]| + |R_L E[J(\boldsymbol{u}_h)]| \end{aligned} \tag{48}$$

• Variance error bound (Type II):

$$\begin{aligned} |V[J(\boldsymbol{u})] - Q_L V[J(\boldsymbol{u}_h)]| \leq\ & 2\,(|Q_L E[|\boldsymbol{\varepsilon}_h|^2]| + |R_L E[|\boldsymbol{\varepsilon}_h|^2]|)^{1/2} \\ & \times (|Q_L V[J(\boldsymbol{u}_h)]| + |R_L V[J(\boldsymbol{u}_h)]|)^{1/2} \\ & + |Q_L E[|\boldsymbol{\varepsilon}_h|^2]| + |R_L E[|\boldsymbol{\varepsilon}_h|^2]| + |R_L V[J(\boldsymbol{u}_h)]| \end{aligned} \tag{49}$$

3.3 Estimating the Standard Deviation Error

In Section 6, several example problems are presented that utilize the expectation error estimate Eq. (44) and variance error estimate Eq. (45). In graphing statistics data, the standard deviation (denoted by $\sigma \equiv \sqrt{V[\cdot]}$) is often reported, rather than the variance. When signed realization and quadrature errors are available, the signed standard deviation error can be directly estimated as follows (using the notation of Section 3.1):

$$\begin{aligned} \sqrt{V[J]} - \sqrt{Q_L V[J_h]} &\approx \sqrt{E[\tilde{J}^2] - (E[\tilde{J}])^2} - \sqrt{Q_L E[J_h^2] - (Q_L E[J_h])^2} \\ &= \sqrt{Q_L E[\tilde{J}^2] + R_L E[\tilde{J}^2] - (Q_L E[\tilde{J}] + R_L E[\tilde{J}])^2} - \sqrt{Q_L E[J_h^2] - Q_L^2 E[J_h]} \end{aligned} \tag{50}$$

When only the magnitudes of realization QOI error and the quadrature error are known, the following approximation can be used:

$$|\sqrt{V[J]} - \sqrt{Q_L V[J_h]}| \approx \frac{|V[J] - Q_L V[J_h]|}{2\sqrt{Q_L V[J_h]}} \tag{51}$$

where $|V[J] - Q_L V[J_h]|$ is calculated using Eq. (49), which only requires the magnitude of realization and quadrature errors.

4 A Software Framework for Non-Intrusive Uncertainty Propagation with Computable Error Bounds

A non-intrusive uncertainty propagation framework with optional error bounds is summarized in the Figure 5 flowchart. A user first specifies sources of uncertainty, provides realizations for outputs of interest, $J(u_h(\boldsymbol{x},t;\boldsymbol{\xi}^{(i)});\boldsymbol{\xi}^{(i)})$, and optionally provides an estimate of the error, $|J(u(\boldsymbol{x},t;\boldsymbol{\xi}^{(i)});\boldsymbol{\xi}^{(i)}) - J(u_h(\boldsymbol{x},t;\boldsymbol{\xi}^{(i)});\boldsymbol{\xi}^{(i)})|, i = 1,\ldots,N$.

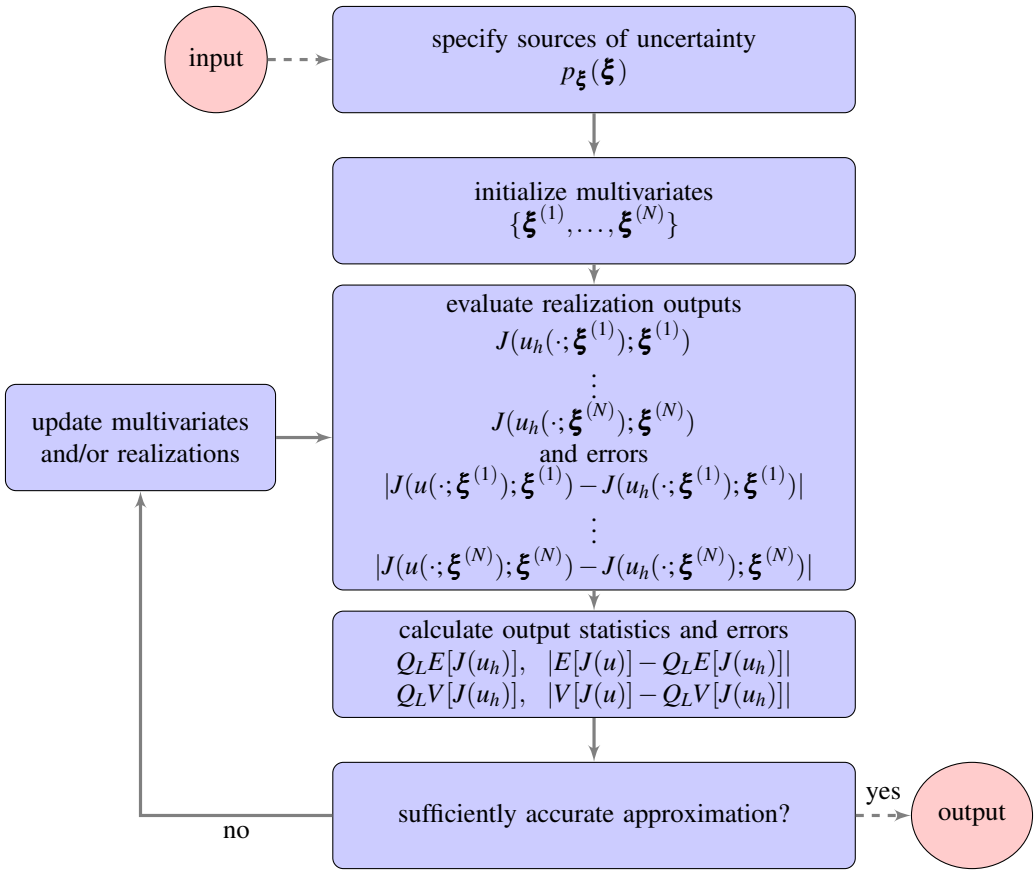

Figure 5. Flowchart of the generalized non-intrusive uncertainty propagation framework.

5 Estimating the Probability Density for Output Quantities of Interest

Output probability density distributions that deviate significantly from a normal distribution are not well characterized by expectation and variance. In this situation, it is often preferable to actually construct an approximation to the output QOI probability density distribution. Kernel density estimation is a standard technique in statistics that is used for this purpose.

5.1 Kernel Density Estimation

Kernel density estimation (KDE) is an algorithm attributed to Rosenblatt [33] and Parzen [28] for estimating the probability density distribution of an independent and identically distributed (i.i.d.) population of samples. Specifically, given a set of M i.i.d. samples $\{x_1, x_2, \ldots, x_M\}$, the probability density distribution is estimated from the sum:

$$p(x) = \frac{1}{Mh} \sum_{i=1}^{M} K\left(\frac{x - x_i}{h}\right) \tag{52}$$

where there is flexibility in the choice of kernel $K(\cdot)$ and bandwidth h. A popular choice is the Gaussian kernel:

$$K(x) = \frac{1}{\sqrt{2\pi}} e^{-\frac{1}{2}|x|^2} \tag{53}$$

with bandwidth h calculated from the population standard deviation σ and cardinality M:

$$h = \left(\frac{4\sigma^5}{3M} \right)^{1/5} \tag{54}$$

which is optimal whenever the density being estimated is Gaussian. When M is small, results depend highly on the choice of the bandwidth parameter h and the representation of multi-modal probability density distributions is generally poor. As the sample population cardinality M increases, observe that the bandwidth parameter h given by Eq. (54) decreases. In this increasing limit, the resulting probability density distributions become relatively insensitive to h (even for multi-modal probability density distributions). Consequently, our strategy is to first construct a response surface giving the QOI response to changes in parameter samples. The response surface can then be i.i.d. sampled using a large number of samples (usually $M > 10,000$ or larger) at little cost.

5.2 Kernel Density Estimation for Output Quantities of Interest

Given Clenshaw-Curtis or Gauss-Patterson quadrature points at the finest level L:

$$\{\boldsymbol{\xi}^{(1)}, \boldsymbol{\xi}^{(2)}, \cdots, \boldsymbol{\xi}^{(N_L)}\}$$

and output quantities of interest:

$$\{J[u_h(\boldsymbol{x},t;\boldsymbol{\xi}^{(1)})], J[u_h(\boldsymbol{x},t;\boldsymbol{\xi}^{(2)})], \cdots, J[u_h(\boldsymbol{x},t;\boldsymbol{\xi}^{(N_L)})]\}$$

a response surface is constructed that provides fast approximate evaluation of $J[u_h(\boldsymbol{x},t;\boldsymbol{\xi})]$ using either of the following interpolants:

- Dense tensor product WENO polynomial interpolants [22, 8] using data at Clenshaw-Curtis or Gauss-Patterson quadrature points. These polynomials are already constructed in the HYGAP method so the cost can be minimal.
- Sparse tensor product interpolants [11] using data at sparse tensor product Clenshaw-Curtis or Gauss-Patterson quadrature points.

Once the response surface has been constructed, the cost associated with obtaining a large population of i.i.d. samples is minimal. Using a large population yields high-quality results even for multi-modal probability density distributions.

5.3 Correcting Kernel Density Estimates Using Realization Error

Results presented in Section 6 present probability density distributions for output QOIs that were calculated using KDE via a response surface sampling. Obtaining error bound estimates for probability density distributions that are calculated using KDE via response surface is a complex task

not discussed here. Instead, Section 6 results also show "realization error corrected" probability density distributions that are obtained by first constructing a response surface using output QOI data that has been corrected using an estimate of the realization error, i.e., $J[u_h(\boldsymbol{x},t;\boldsymbol{\xi}^{(i)})]+\varepsilon_h$, and then performing KDE using this corrected response surface. This provides an assessment of the impact of realization error on the output QOI probability density distribution.

Note that in adding realization error as a correction, one often observes "systematic biasing" effects, i.e., the corrected probability density distribution is shifted. This effect is easily understood since adding a *constant* ε_0 to expectation data merely shifts the expectation statistic, $E[J_h+\varepsilon_0]=\varepsilon_0+E[J_h]$, and does not change the variance, $V[J_h+\varepsilon_0]=V[J_h]$.

6 Numerical Applications

Several numerical examples have been selected to demonstrate the capabilities outlined in this article. These examples are briefly summarized in Table 3. Problems using Richardson ($r=2$) or Aitken extrapolation to estimate realization error require CFD simulations using 2 or 3 mesh resolutions, respectively. The multi-element airfoil problem uses a dual problem to estimate the realization error. For each problem, kernel density estimation (KDE), discussed in Section 5, was used to calculate a probability density distribution for the lift coefficient and a drag coefficient for the viscous flow problems.

Table 3. Summary of uncertainty calculations.

Section	Flow Problem	Uncertainty Type	Realization Error	Quadrature
6.1.1	2-D airfoil	boundary condition parameters	Aitken extrapolation	dense
6.1.2	2-D airfoil	turbulence model parameters	Aitken extrapolation	dense
6.2	3-D wing-body	slat and flap geometry	Aitken extrapolation	dense/sparse
6.3	3-D wing	boundary condition parameters	Aitken extrapolation	dense
6.4	3-D launch vehicle	thrust parameter	Richardson extrapolation	dense
6.5	2-D 3-element airfoil	boundary condition parameter	dual problem	dense
6.6	2-D airfoil	correlated random field	Aitken extrapolation	dense/sparse

6.1 NACA 0012 Airfoil Flow Computations with Uncertainty

Steady-state Reynolds-averaged Navier-Stokes (RANS) flow over a NACA 0012 airfoil geometry was calculated using a finite-volume method that achieves second-order spatial accuracy using linear polynomial MUSCL reconstruction [40, 41]. The one-equation Baldwin-Barth [3] turbulence model was used to model the effects of turbulence. Calculations were performed using a hierarchy of three structured meshes containing 513×65, 257×33, and 129×17 mesh points.

Experimental data from Harris [19] is available for comparison at a Mach number of 0.8, angle-of-attack (AOA) of 2.26°, and a Reynolds number of 9×10^6. These transonic flow conditions, as depicted in Figure 6, were chosen because computations utilizing the RANS equations with various

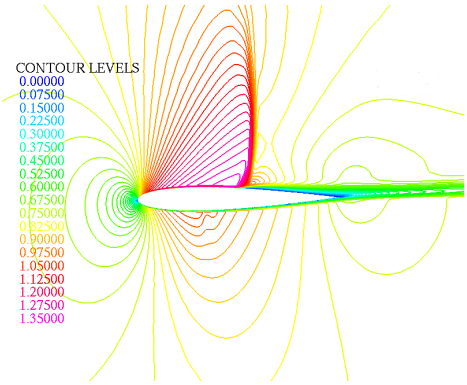

Figure 6. RANS flow over a NACA 0012 airfoil. Mach number contours from a single realization calculation at $M_\infty = 0.8$ and $AOA = 2.26^\circ$.

turbulence models show sensitivity to flow conditions and turbulence model parameters, yet no single value of these parameters fits the experimental data very well. This makes the flow problem an excellent candidate for uncertainty analysis. In subsequent calculations, three different forms of uncertainty for this flow problem are considered:

- Section 6.1.1: Uncertainty in the inflow boundary Mach number and angle-of-attack parameters.
- Section 6.1.2: Uncertainty in 3 Baldwin-Barth turbulence model parameters.
- Section 6.6: Uncertainty in the inflow boundary Mach number profile, modeled as a correlated random field.

6.1.1 NACA 0012 Airfoil Flow with Inflow Uncertainty

Uncertainty in the inflow Mach number and angle-of-attack (AOA) were imposed using Gaussian distributions truncated at four standard deviations and normalized to have unit total probability

- $M_\infty = \text{Gaussian}_{4\sigma}(m = 0.8, \sigma = .01)$
- $AOA = \text{Gaussian}_{4\sigma}(m = 2.26^\circ, \sigma = 0.1^\circ)$

Uncertainty statistics for output QOIs were then calculated using the Clenshaw-Curtis HYGAP approximation discussed in Section 2.5.3. Pressure coefficient statistics and Type I estimates of total error on the airfoil surface are graphed in Figure 7. The calculation using $L = 4$ Clenshaw-Curtis quadrature requires 81 CFD evaluations for each mesh resolution in the hierarchy of CFD meshes. Overall, the level of error in mean and standard deviation statistics is rather small except within the upper surface shock wave profile and immediately downstream of the shock wave. For the particular flow conditions chosen, this figure also shows the surprisingly large uncertainty in lower surface pressure coefficient values. This is apparently due to the presence of a weak lower surface shock wave that is sometimes present when the uncertainty parameters are varied. The presence of a lower surface shock wave significantly changes the solution and arguably explains

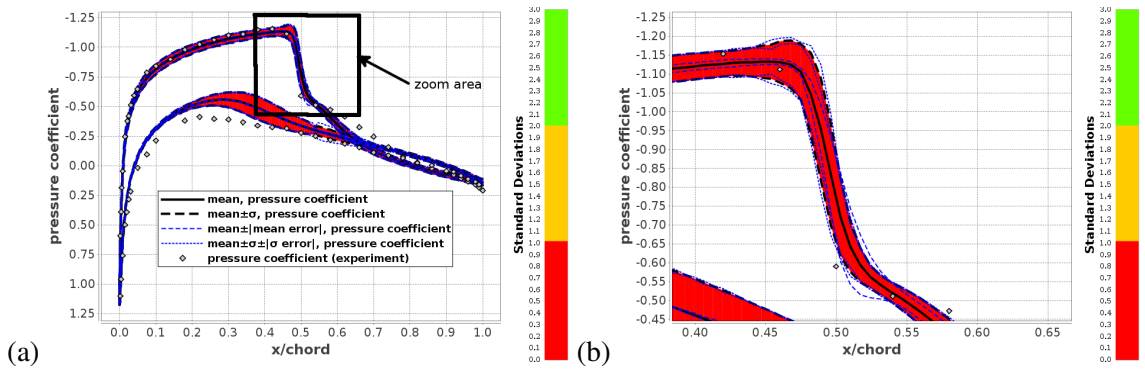

Figure 7. Surface pressure coefficient statistics on the NACA 0012 airfoil surface for transonic flow with inflow Mach number and AOA uncertainty. Shown are mean and standard deviation statistics as well as the estimates of mean and standard deviation errors for (a) the entire airfoil and (b) a closeup in the upper surface shock region.

the relatively large uncertainty in the lower surface pressure distribution. More fundamentally, the appearence of a strong shock wave on the upper surface and a weak lower surface shock wave that depend on values of the random parameters may cause the random variable data to be non-smooth in these locations. For non-smooth random variable data, the Clenshaw-Curtis HYGAP algorithm switches from standard global Clenshaw-Curtis quadrature to piecewise polynomial approximated quadrature using the Clenshaw-Curtis quadrature point data.

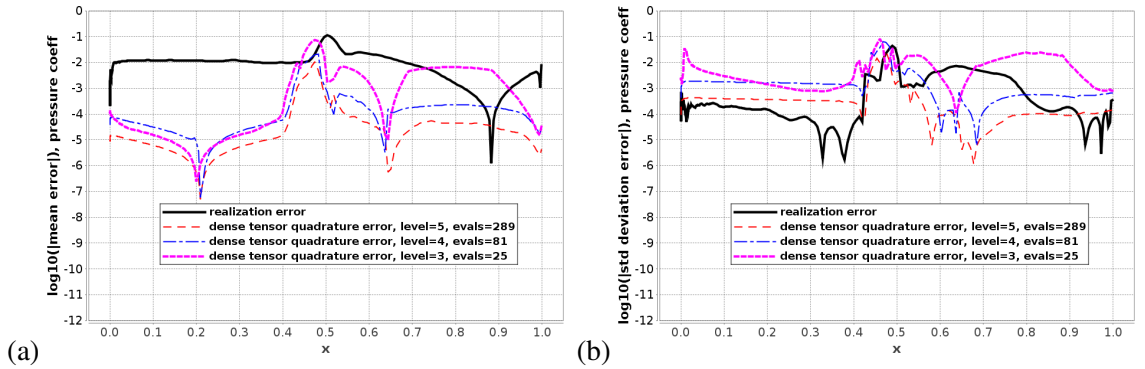

Figure 8. Statistics errors on the upper surface of the NACA 0012 airfoil for transonic flow with inflow Mach number and AOA uncertainty. Shown are Type I estimates of realization error and quadrature errors using $L = 3, 4, 5$ Clenshaw-Curtis HYGAP quadrature for the (a) mean and (b) standard deviation.

Figures 8 and 9 show graphs for Type I and Type II estimates of mean and standard deviation error for this uncertainty calculation. The Type I error estimates do not rely on inequality estimates, and consequently are generally assumed to be sharper than Type II error bound estimates. Realization and quadrature error curves for $L = 3, 4, 5$ HYGAP Clenshaw-Curtis quadrature are shown in figures 8 and 9 for comparison. The realization error curves are obtained by artificially setting the quadrature error equal to zero. Similarly, the quadrature error curves are obtained by artificially setting the realization error equal to zero. When compared to the Type I realization error estimates, the Type I quadrature error estimates from both $L = 4$ and $L = 5$ Clenshaw-Curtis HYGAP approximations appear acceptable. The criteria for acceptability used here assumes that the realization error from the CFD calculations is given and the quadrature error should balance or be less than (but perhaps

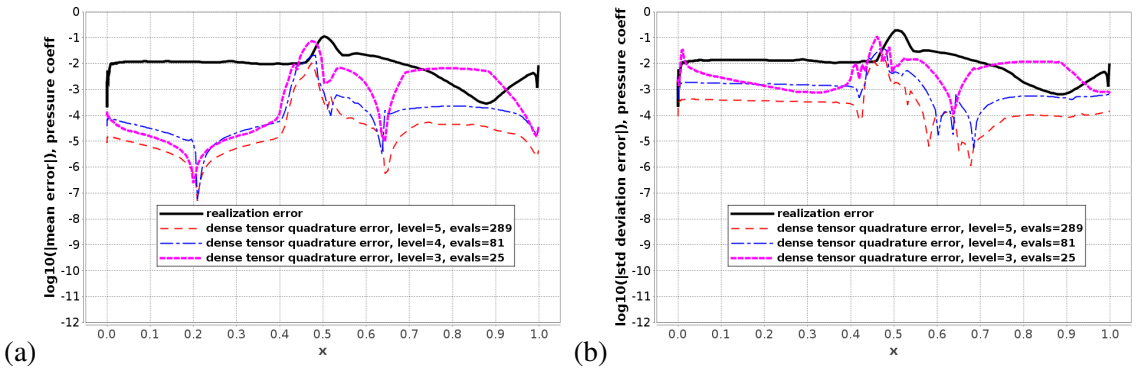

Figure 9. Statistics errors on the upper surface of the NACA 0012 airfoil for transonic flow with inflow Mach number and AOA uncertainty. Shown are Type II estimates of realization error and quadrature errors using $L = 3,4,5$ Clenshaw-Curtis HYGAP quadrature for the (a) mean and (b) standard deviation.

not strictly less than) the realization error. The computational savings in using $L = 4$ approximation is substantial since for two sources of uncertainty it requires only 81 CFD evaluations as compared to $L = 5$, which requires 289 CFD evaluations. Figure 10 graphs the probability density functions

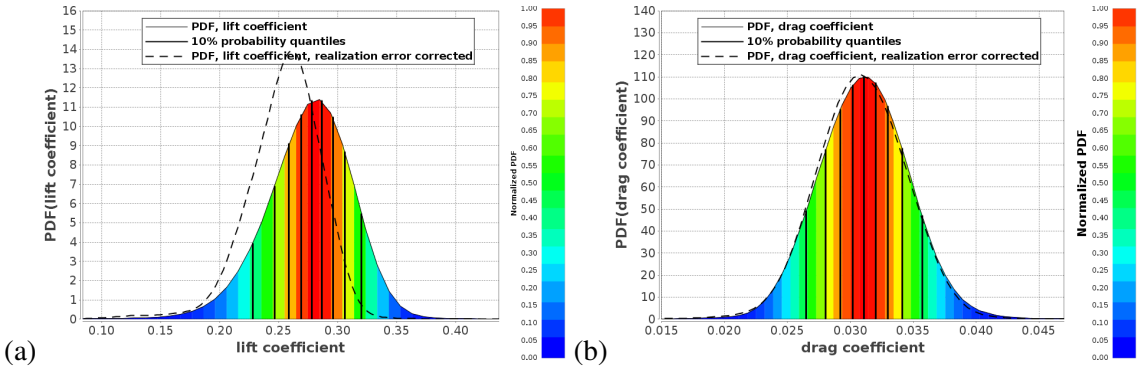

Figure 10. Probability density distributions for (a) lift coefficient and (b) drag coefficient for transonic flow over the NACA 0012 geometry with inflow Mach number and AOA uncertainty.

for lift and drag coefficients using the kernel density estimation procedure discussed in Section 5. In addition, this figure graphs the probability density function corrected by realization error, also discussed in Section 5. All distributions have a near-normal (Gaussian) shape. Surprisingly, the lift coefficient distribution seems most heavily impacted by the realization error with only a minor impact seen in the drag coefficient distribution.

6.1.2 NACA 0012 Airfoil Flow with Turbulence Model Parameter Uncertainty

The computations of the previous example are now repeated with uncertainty imposed in parameters of the Baldwin-Barth [3] turbulence model. Given a fluid density ρ, velocity components $u_i, i = 1,\ldots,d$ from the RANS approximation, and a wall distance y^+, the Baldwin-Barth turbulence model is a one-equation PDE of the form:

$$\frac{DR_T}{Dt} = (c_{\varepsilon_2} f_2(y^+) - c_{\varepsilon_1})\sqrt{R_T P} + (\nu + \frac{\nu_T}{\sigma})\nabla^2 R_T - \frac{1}{\sigma}(\nabla \nu_t)\cdot \nabla R_T \tag{55}$$

where

$$\mu_T = \rho \nu_T = \rho c_\mu D_1(y^+) D_2(y^+) R_T \quad , \quad P = \nu_T \left(\frac{\partial u_i}{\partial x_j} + \frac{\partial u_j}{\partial x_i} \right) \frac{\partial u_i}{\partial x_j} - \frac{2}{3} \nu_T \left(\frac{\partial u_k}{\partial x_k} \right)^2$$

$$D_1 = 1 - \exp(-y^+/A^+) \quad , \quad D_2 = 1 - \exp(-y^+/A_2^+), \quad \sigma^{-1} = (c_{\varepsilon_2} - c_{\varepsilon_1}) \sqrt{c_\mu} / \kappa^2$$

and

$$\begin{aligned} f_2(y^+) \quad = \quad & \frac{c_{\varepsilon_1}}{c_{\varepsilon_2}} + (1 - \frac{c_{\varepsilon_1}}{c_{\varepsilon_2}})(\frac{1}{\kappa y^+} + D_1 D_2) \\ & \times \left(\sqrt{D_1 D_2} + \frac{y^+}{\sqrt{D_1 D_2}} (\frac{1}{A^+} \exp(-y^+/A^+) D_2 + \frac{1}{A_2^+} \exp(-y^+/A_2^+) D_1) \right) \end{aligned}$$

with reference model parameters $\kappa = .41, c_\mu = .09, c_{\varepsilon_1} = 1.2, c_{\varepsilon_2} = 2.0, A^+ = 26$, and $A_2^+ = 10$ as given in Baldwin and Barth [3]. Uncertainty is imposed in three parameters of the model that are often observed to be most sensitive:

- $c_\mu = \text{Uniform}[.081, .099]$
- $c_{\varepsilon_1} = \text{Uniform}[1.08, 1.32]$
- $c_{\varepsilon_2} = \text{Uniform}[1.8, 2.2]$

Uncertainty statistics for output QOIs were then calculated using the Clenshaw-Curtis HYGAP approximation discussed in Section 2.5.3. The calculation using the $L = 4$ Clenshaw-Curtis quadrature

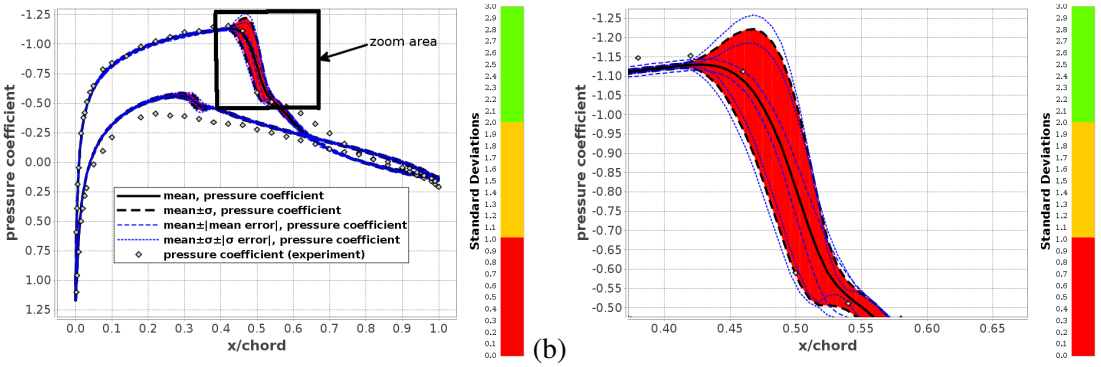

Figure 11. Surface pressure coefficient statistics on the NACA 0012 airfoil surface for transonic flow with Baldwin-Barth turbulence model uncertainty. Shown are mean and standard deviation statistics as well as the estimates of mean and standard deviation errors for (a) the entire airfoil and (b) a closeup in the upper surface shock region.

with three sources of uncertainty requires 729 CFD evaluations for each mesh resolution in the hierarchy of CFD meshes. Pressure coefficient statistics and Type I error estimates on the airfoil surface are graphed in Figure 11. In contrast to the previous example, the uncertainties remain somewhat confined to the upper shock profile region with only very small uncertainties seen on the lower surface. Type I and Type II pressure coefficient error estimates are shown in figures 12 and 13. Using the criteria of Section 6.1.1, examination of the errors in mean and standard deviation graphed in

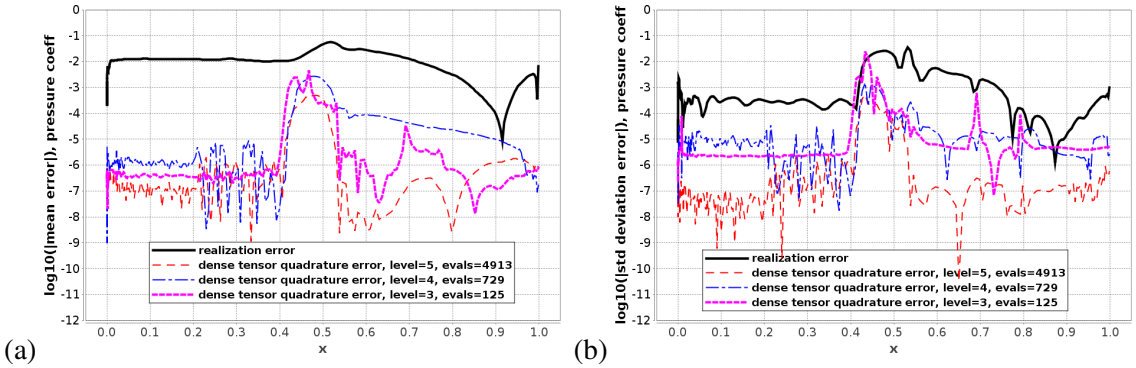

Figure 12. Statistics errors on the upper surface of the NACA 0012 airfoil for transonic flow with Baldwin-Barth turbulence model uncertainty. Shown are Type I estimates of realization error and quadrature errors using $L = 3,4$ Clenshaw-Curtis HYGAP quadrature for the (a) mean and (b) standard deviation statistic.

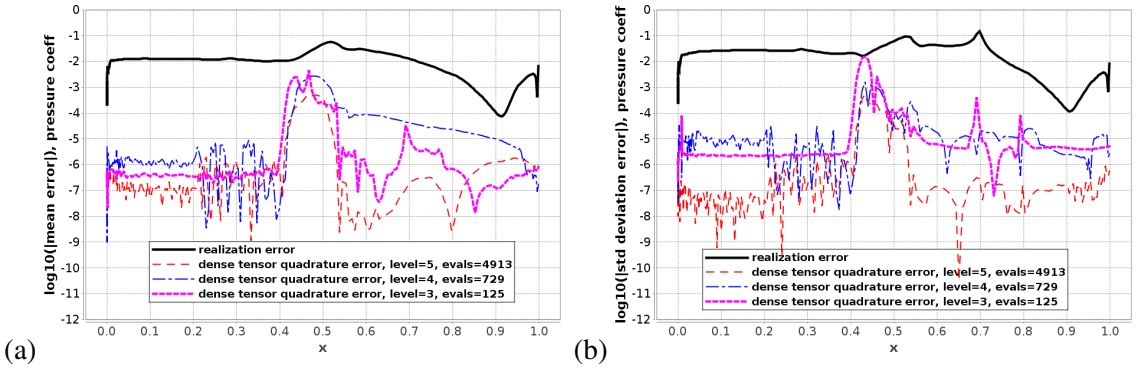

Figure 13. Statistics errors on the upper surface of the NACA 0012 airfoil for transonic flow with Baldwin-Barth turbulence model uncertainty. Shown are Type II estimates of realization error and quadrature errors using $L = 3,4$ Clenshaw-Curtis HYGAP quadrature for the (a) mean and (b) standard deviation statistic.

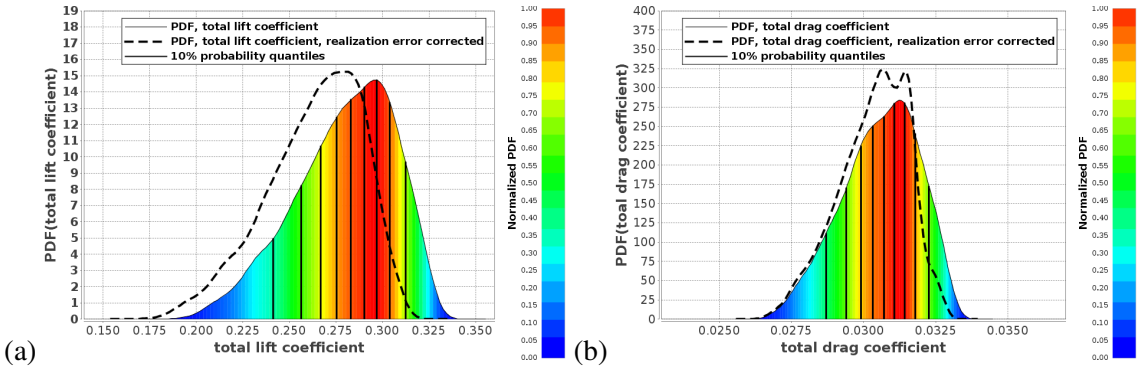

Figure 14. Probability density distributions for (a) lift coefficient and (b) drag coefficient for transonic flow over the NACA 0012 geometry with Baldwin-Barth turbulence model uncertainty.

Figure 12 indicate that the $L = 3$ Clenshaw-Curtis HYGAP approximation using just 125 CFD evaluations at each CFD mesh resolution may be sufficient. Figure 14 graphs the probability density

distributions for lift and drag coefficients with and without realization error correction, as discussed in Section 5. These graphs do show a non-negligible impact of realization error on the probability density distributions for both lift and drag. Observe that although the input uncertainty distributions for turbulence model parameters are uniform distributions, the resulting output distributions have a more peaked Gaussian shape. This has significant meaning. The input probability laws for model parameters were all chosen as uniform probability density distributions. This implies for each parameter that all possible values in an interval have equal probability. The observed output probability density is a peaked distribution, which implies that this output is relatively insensitive to the uncertain model parameters. This form of input-output response is often sought in the design of model systems.

6.2 High-Lift Wing-Body Flow with Slat and Flap Geometric Uncertainty

Steady-state Reynolds-averaged Navier-Stokes flow over a high-lift wing-body geometry at Mach 0.2 and angle-of-attack 13° was computed using the OVERFLOW [21] CFD solver. This test case is taken from the 1st AIAA CFD High Lift Prediction Workshop [36] held in 2010. Details of the OVERFLOW calculations presented at that workshop can be found in Sclafani *et al.* [35]. Experimental data from NASA Langley Research Center wind tunnel testing is available for comparison.

In the present calculations, uncertainty in the slat and flap angles has been imposed:

- $\alpha_{\text{slat}} = 30^\circ + \text{Gaussian}_{4\sigma}(m = 0.0^\circ, \sigma = .75^\circ)$
- $\alpha_{\text{flap}} = 25^\circ + \text{Gaussian}_{4\sigma}(m = 0.0^\circ, \sigma = .75^\circ)$

A hierarchy of refined CFD mesh resolutions was used in calculations so that realization errors can be estimated using Aitken extrapolation. The finest resolution meshes contain approximately 90 million mesh points. Figure 15 shows surface pressure contours from a single OVERFLOW

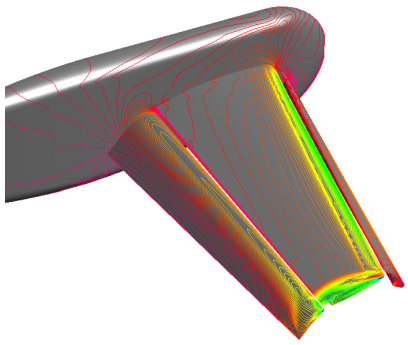

Figure 15. Surface pressure coefficient contours on the NASA Trap Wing high-lift model with inflow conditions $M_\infty = 0.2$, $AOA = 13^\circ$ with slat deployed 30° and slat deployed 25°. Green denotes low values and red denotes high values.

calculation with slat deployed 30° and slat deployed 25°. Uncertainty statistics for output QOIs

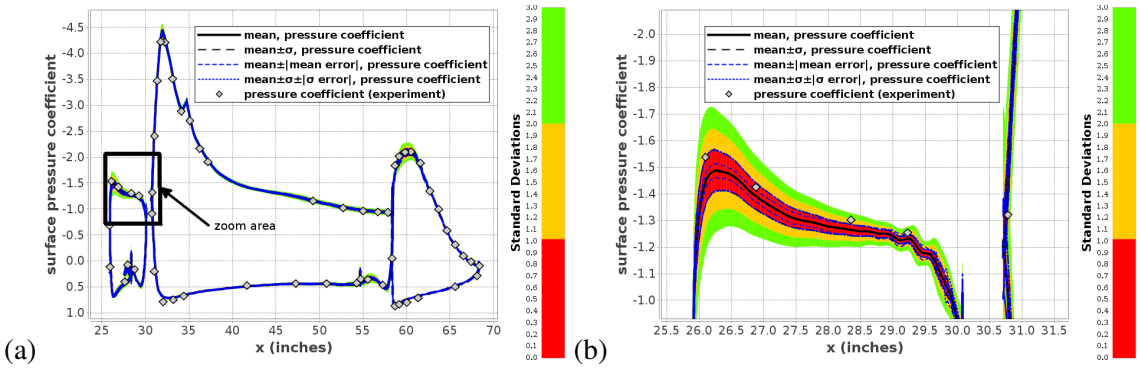

Figure 16. Surface pressure coefficient statistics at the 50% wing span location for the NASA Trap Wing high-lift model with slat and flap angle uncertainty. Shown are mean and standard deviation statistics as well as the estimates of mean and standard deviation errors for (a) entire wing section and (b) a closeup in the slat region.

were calculated using Clenshaw-Curtis quadrature points in dense and sparse tensor product form. The calculation using $L = 4$ Clenshaw-Curtis dense tensor product quadrature requires 81 CFD evaluations and the sparse tensor product quadrature requires 29 CFD evaluations for each mesh resolution in the hierarchy. Surface pressure statistics and errors at the 50% wing span location are shown in Figure 16. The uncertainties appear to be quite small everywhere except the leading

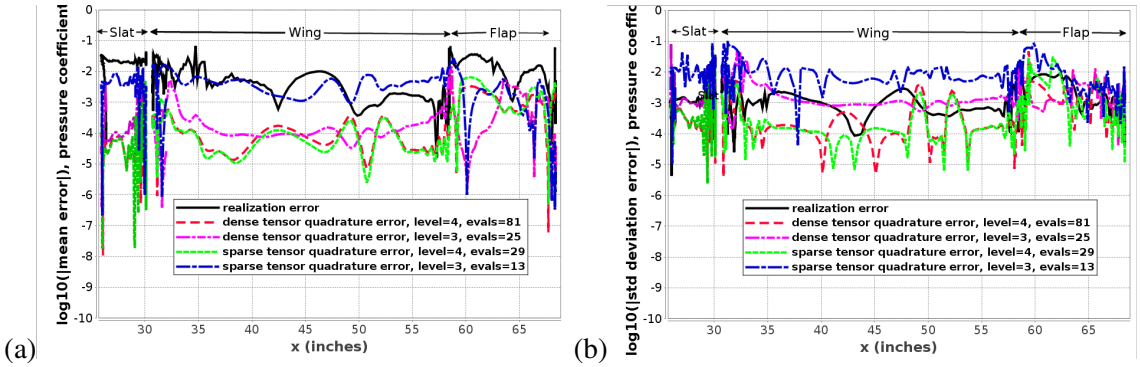

Figure 17. Statistics errors on the upper surface of the NASA Trap Wing high-lift model with slat and flap angle uncertainty. Shown are realization error and quadrature errors using $L = 3,4$ sparse and dense tensor product forms of Clenshaw-Curtis quadrature for the (a) mean and (b) standard deviation.

edge slat and near the leading edge of the flap. Figure 17 shows realization error and quadrature error for the mean and standard deviation statistics on the upper surface of the wing at 50% span using both sparse and dense tensor product forms of Clenshaw-Curtis quadrature for $L = 3$ and $L = 4$ approximation. When compared to the realization error, all the quadratures except the $L = 3$ sparse tensor product quadrature have acceptable levels of error. The $L = 4$ sparse tensor product quadrature requires just 29 CFD realization evaluations for each mesh resolution and seems to be a good choice for this problem.

Figure 18 shows the probability density distributions for lift and drag coefficients with and without realization error correction, as discussed in Section 5. These graphs show the non-negligible effect

of realization error on the probability density distributions for both lift and drag. When compared to the lift probability density distribution, the flatness in the drag probability density distribution indicates that the drag is slightly more sensitive to changes in slat and flap angle.

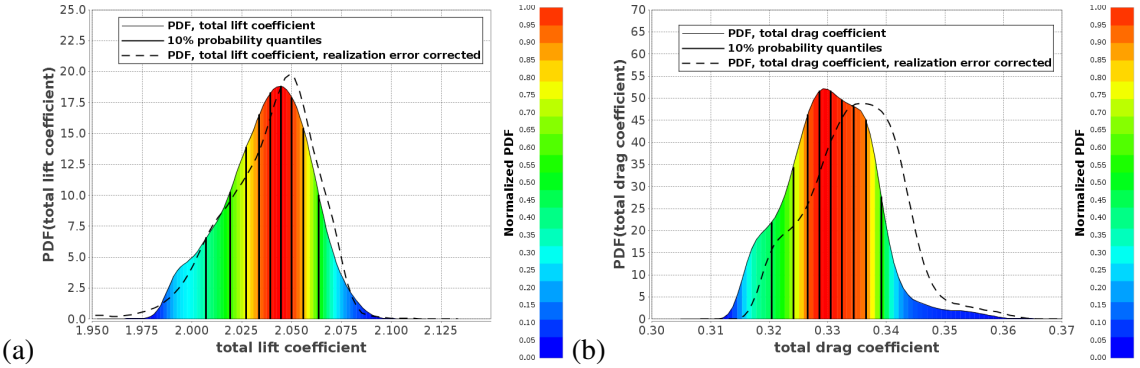

Figure 18. Probability density distributions for (a) lift coefficient and (b) drag coefficient for the NASA Trap Wing high-lift model with slat and flap angle uncertainty.

6.3 ONERA M6 Wing Flow with Uncertain Inflow Conditions

Steady-state Reynolds-averaged Navier-Stokes flow over an ONERA M6 wing at a Reynolds number of 11.72×10^6 was computed using the OVERFLOW [21] CFD solver. Experimental data by Schmitt and Charpin [34] is available for comparison. Uncertainty in the inflow Mach number and angle-of-attack (AOA) were imposed, i.e.:

- $M_\infty = \text{Gaussian}_{4\sigma}(m = .84, \sigma = .02)$
- AOA = $\text{Gaussian}_{4\sigma}(m = 3.06^\circ, \sigma = .075^\circ)$

Calculations were performed on a hierarchy of refined meshes containing approximately 5 million mesh points at the finest resolution. Uncertainty statistics were calculated using $L = 4$ Clenshaw-Curtis HYGAP approximation, defined in Section 2.5.3, which uses Clenshaw-Curtis quadrature for smooth random variable data and cubic piecewise polynomials for non-smooth random variable data. Density and pressure coefficient contours from a single numerical realization at $M_\infty = .84$, $AOA = 3.06^\circ$ are presented in Figure 19. The well-known lambda shock pattern is clearly seen on the upper wing surface. Pressure coefficient statistics and Type I error estimates on the wing surface at the 65% span location are graphed in Figure 20. Significant uncertainties are observed on the upper surface of the wing at the lambda shock and leading edge locations with almost no uncertainty seen in the lower surface. Type I and Type II realization and quadrature error estimates for mean and standard deviation are shown in figures 21 and 22 for $L = 3, 4, 5$ Clenshaw-Curtis HYGAP approximations. Based on results from Figure 21, $L = 4$ approximation using 81 CFD evaluations for each mesh resolution results in a level of error comparable to the realization error and appears to be an acceptable choice for this calculation. To understand these results in more detail, kernel density estimation was used to construct the actual probability density distribution for surface

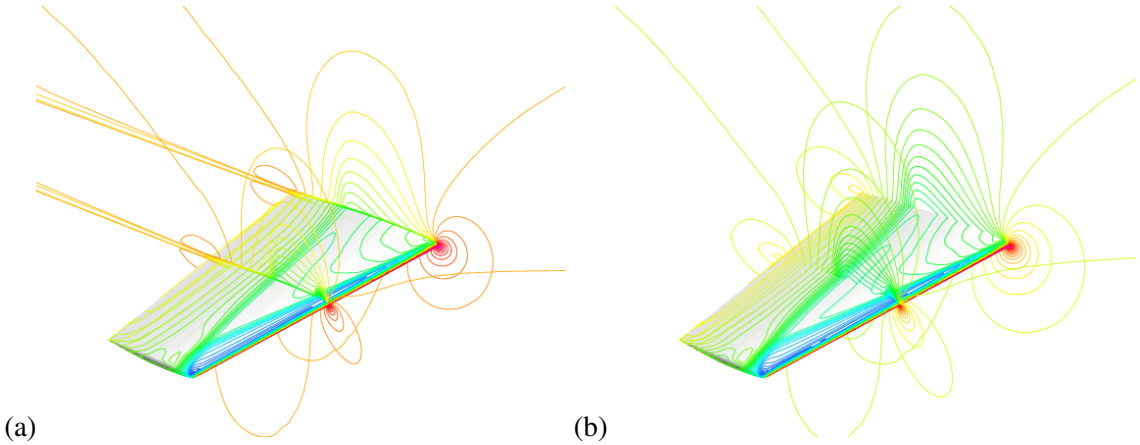

(a) (b)

Figure 19. Transonic Reynolds-averaged Navier-Stokes flow over the ONERA M6 wing at Mach .84 and AOA = 3.06°. Shown are single realization (a) density contours and (b) pressure coefficient contours. Blue denotes low values and red denotes high values.

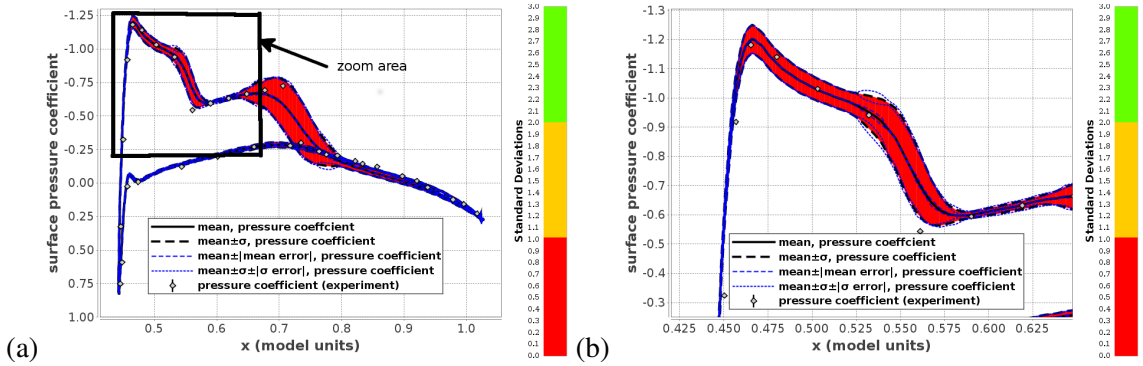

(a) (b)

Figure 20. Surface pressure coefficient statistics at the 65% wing span location for the ONERA M6 wing problem with Mach number and AOA uncertainty. Shown are mean and standard deviation statistics as well as the estimates of mean and standard deviation errors for (a) entire wing section and (b) a closeup in the slat region.

pressure coefficient at each location of the wing surface at the 65% wing span location. Figure 23(a) shows the surface pressure coefficient probability density distribution over the entire wing section, but this probability distribution only has meaning when traversed vertically for a particular x location on the upper or lower surface. Figure 23(b) shows the resulting probability density distribution near the leading edge at $x = 0.5$ on the upper surface. This distribution is very well approximated by a Gaussian distribution, which justifies the use of mean and standard deviation to characterize it. Figure 23(c) shows the surface pressure coefficient probability density distribution at the location of the rear shock wave at $x = 0.722$. The bi-modal shape of this probability density distribution gives high probability to the pre-shock and post-shock states observed in realizations. The standard deviation σ at this location is approximately one-half the distance *between* peaks in the bi-modal distribution and does not characterize the width of any peak. Consequently, any model optimization procedure that seeks to minimize σ for this QOI may be drastically misled. Figure 24 graphs the probability density distributions for lift and drag coefficients with and without realization error correction. The left shifting of corrected distributions is due to the systematic bias that is expected

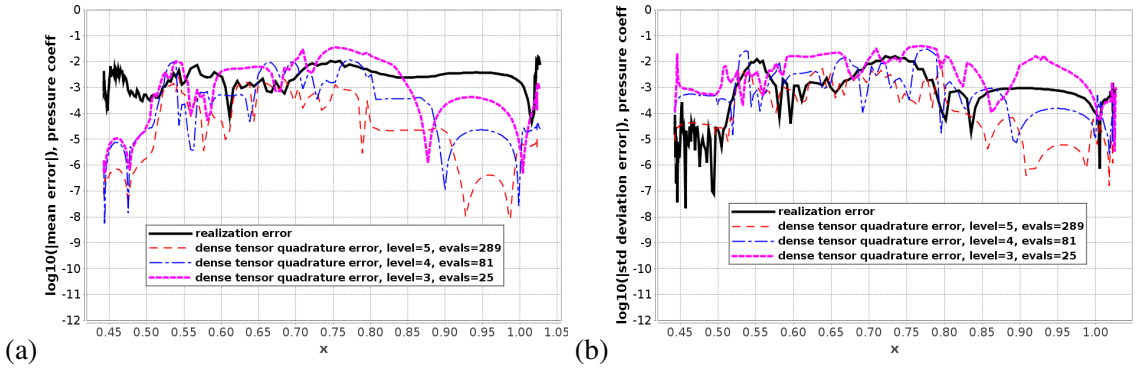

Figure 21. Statistics errors on the wing upper surface for the ONERA M6 wing problem with Mach number and AOA uncertainty. Shown are Type I estimates of realization error and quadrature errors using $L = 3,4,5$ dense tensor product forms of Clenshaw-Curtis quadrature for the (a) mean and (b) standard deviation.

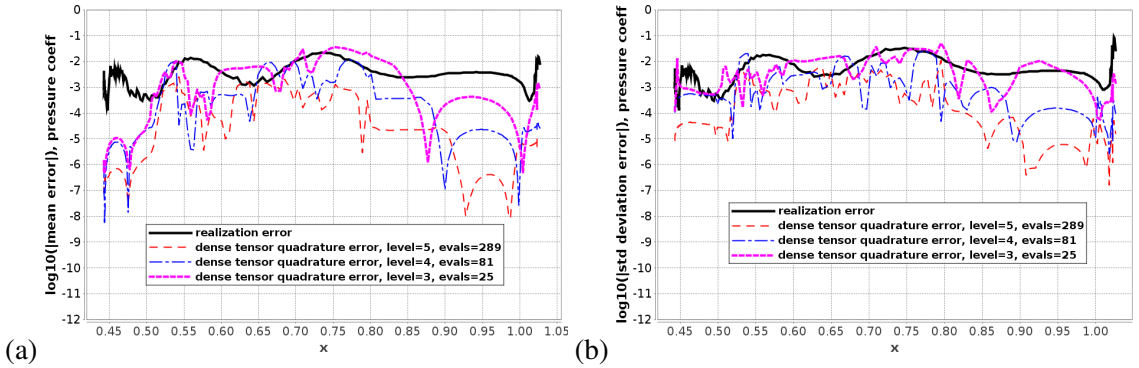

Figure 22. Statistics errors on the wing upper surface for the ONERA M6 wing problem with Mach number and AOA uncertainty. Shown are Type II estimates of realization error and quadrature errors using $L = 3,4,5$ dense tensor product forms of Clenshaw-Curtis quadrature for the (a) mean and (b) standard deviation.

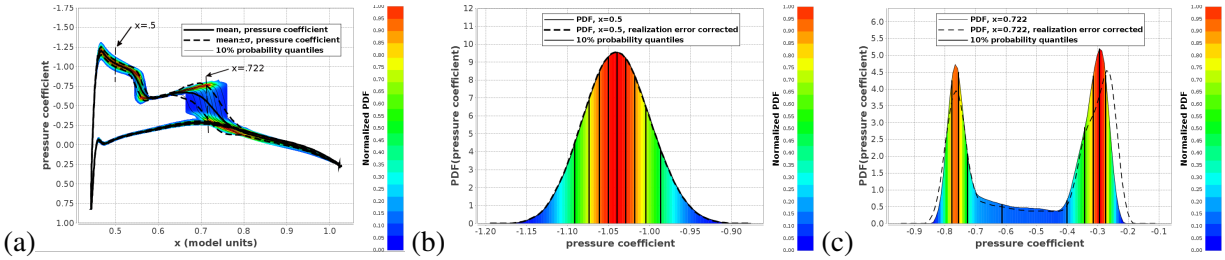

Figure 23. Surface pressure coefficient statistics at the 65% wing span location for the ONERA M6 wing problem with Mach number and AOA uncertainty. Shown are a color shaded probability density function with 10% quantile partititions for (a) the entire wing section, (b) at the location $x = .5$ on the upper surface, and (c) at the shock wave location $x = .722$ on the upper surface.

from realization error corrections, as discussed in Section 5. Given that the input probability laws for Mach number and angle-of-attack where chosen to be Gaussian distributions, the near Gaussian shape of lift, and the skewed Gaussian shape of drag may be interpreted as meaning that lift is

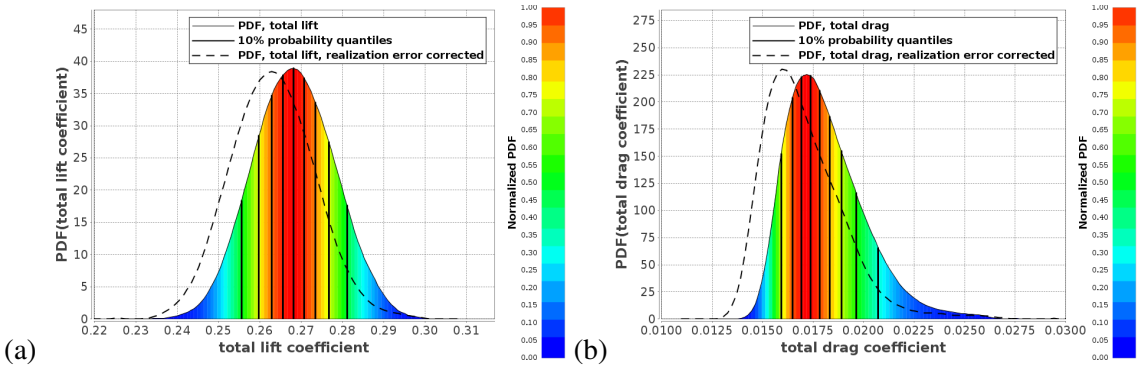

Figure 24. Probability density distributions for (a) lift coefficient and (b) drag coefficient for the ONERA M6 wing problem with Mach number and AOA uncertainty.

responding nearly linearly to variations in the uncertain parameters while drag is not.

6.4 Launch Vehicle Plume Analysis with Uncertain Thrust

In this example, uncertainty propagation for a launch vehicle simulation with exhaust plume modeling is considered. Launch vehicle designs must cope with very large forces, volatile chemicals,

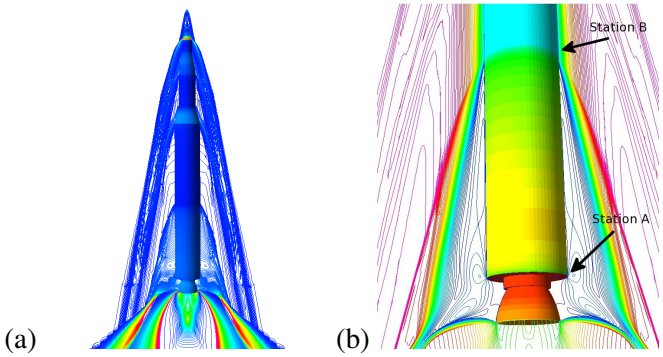

Figure 25. Mach 6.7 flow over a launch vehicle configuration with rocket plume modeling. Shown are (a) pressure contours over the entire launch vehicle and (b) contours of flow field Mach number and surface color shading of flow field density in the lower rocket region. Blue denotes low values and red denotes high values.

and extremely hot rocket plume gases. A phenomenon sometimes encountered in these designs is Plume Induced Flow Separation (PIFS). As an example of this phenomenon, Figure 25(a) shows Mach 6.7 flow over a launch vehicle with rocket plume modeling approximated using the OVERFLOW [21] CFD solver (courtesy Goetz Klopfer, NASA Ames). As the launch vehicle accelerates and ascends into the atmosphere, the rocket plume expands and eventually causes the flow to separate near Station B on the rocket body with reversed flow occurring between Stations A and B in Figure 25(b). This reversed flow may carry hot plume gases in close proximity to the rocket body, resulting in material failure unless additional thermal protection is provided. As a historical

note, this phenomenon was encountered in the NASA Apollo Saturn-V launches during 1967-1973. Consequently, during those launches one of the five Saturn-V engines was intentionally powered off at a prescribed altitude to reduce the severity of the PIFS phenomenon. For the present simplified single-engine configuration, calculations were performed to quantify the extent of the PIFS flow reversal with respect to uncertain flight Mach number and thrust conditions, i.e.:

- $M_\infty = \text{Gaussian}_{3\sigma}(m = 6.7, \sigma = .067)$
- $\text{thrust} = \text{Uniform}[\text{thrust}_{80\%}, \text{thrust}_{100\%}]$

where $\text{thrust}_{80\%}$ and $\text{thrust}_{100\%}$ denote thrust at 80% and 100% power settings, respectively. One way to characterize the extent of this reversed flow is via a skin friction coefficient that changes sign when the vertical (streamwise) component of velocity changes direction.

Figure 26 graphs skin friction coefficient statistics and Type I error estimates between Stations A and B using $L = 4$ Clenshaw-Curtis HYGAP approximation using 81 CFD evaluations.

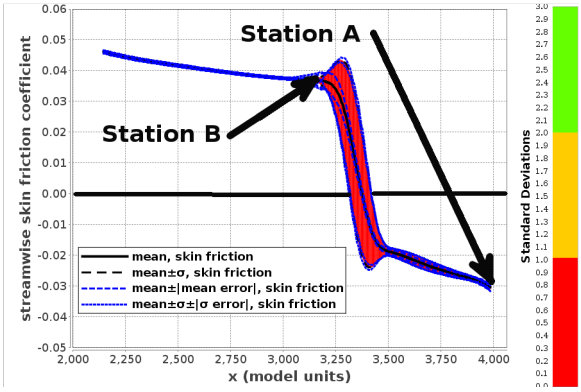

Figure 26. Mach 6.7 flow over a launch vehicle configuration with Mach number and thrust uncertainty. Shown are skin friction coefficient uncertainty statistics and Type I error estimates using $L = 4$ Clenshaw-Curtis HYGAP uncertainty approximation.

The mean streamwise skin friction component becomes negative at approximately $x = 3,375$, which indicates flow reversal and flow separation; but there is significant uncertainty in this position due to Mach number and thrust uncertainty. This uncertainty in flow separation and reversal position is the information sought by engineers. Figures 27 and 28 provide graphs of Type I and Type II estimates of mean and standard deviation error in the region between Station A and Station B for this calculation. These figures indicate that the accuracy in these output statistics appears to be dominated by realization error in the CFD computations. This is useful information if more accurate statistics are required because it indicates that additional resources should be first used to improve the accuracy of the CFD realizations and *not* used to improve the accuracy of the statistics integral quadratures until error balancing is achieved.

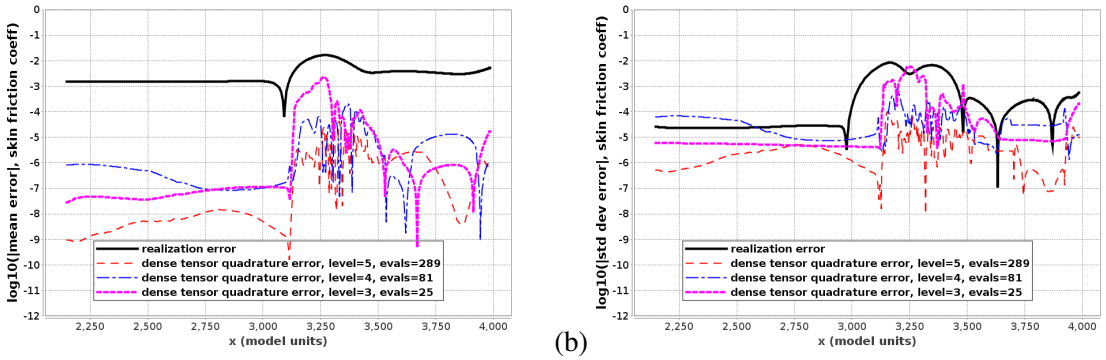

Figure 27. Mach 6.7 flow over a launch vehicle configuration with thrust uncertainty calculated using $L = 3,4,5$ Clenshaw-Curtis HYGAP approximation. Shown are graphs of Type I estimates of skin friction coefficient (a) mean error and (b) standard deviation error between Station A and Station B.

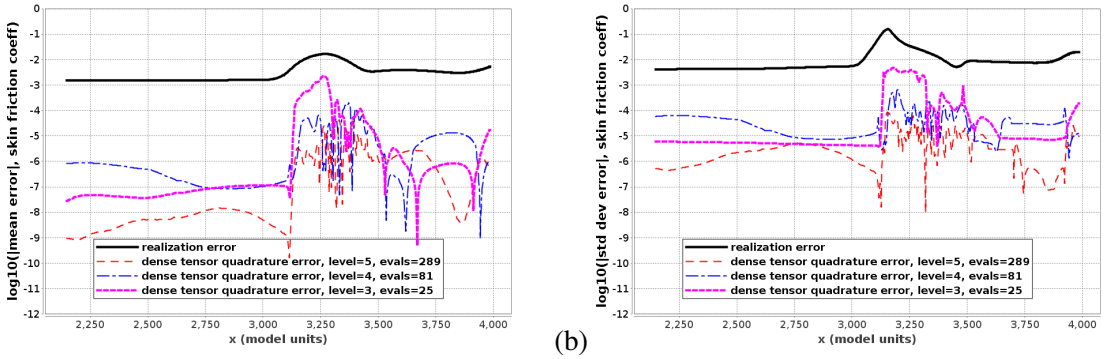

Figure 28. Mach 6.7 flow over a launch vehicle configuration with thrust uncertainty calculated using $L = 3,4,5$ Clenshaw-Curtis HYGAP approximation. Shown are graphs of Type II estimates of skin friction coefficient (a) mean error and (b) standard deviation error between Station A and Station B.

6.5 Inviscid Euler Flow Over a Multi-Element Airfoil with Uncertainty

In this example, steady-state Euler flow over a multi-element airfoil at Mach 0.1 has been computed with angle-of-attack (AOA) uncertainty:

$$AOA = \text{Gaussian}_{4\sigma}(m = 5^\circ, \sigma = 0.1^\circ)$$

Using the theory outlined in Section 2.6.2, a dual problem is used to estimate realization error for the lift coefficient QOI using the error representation equation (35). These dual problems are also used to adaptively refine the mesh using the adaptive refinement indicators in Eq. (37) to reduce the realization error in the lift coefficient QOI. The flow problem was approximated using a discontinuous Galerkin finite-element method [31, 24, 15] formulated in entropy stable symmetric variables as proposed in [4, 5] and used in solving dual problems arising in *a posteriori* error estimation in Larson and Barth [23]. Primal flow problems were computed using linear elements and dual problems were computed using quadratic elements. Figure 29(a) shows Mach number contours of the primal Euler flow problem during the adaptive mesh refinement process and Figure 29(b) shows contours of the dual problem (x-momentum) for the lift coefficient functional. A graph of the error reduction in the lift coefficient during the adaptive meshing process is shown in Figure 30(a) and

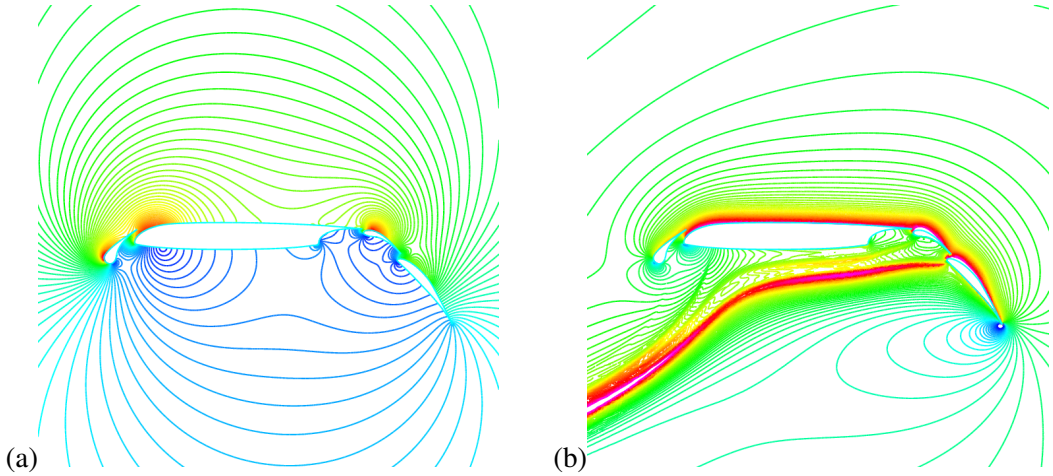

Figure 29. A single realization of Mach 0.1 Euler flow over a multi-element airfoil geometry at 5° AOA. Shown are (a) Mach number contours associated with the primal solution and (b) contours of the x-momentum associated with the dual solution for a lift functional. Blue denotes small values and red denotes large values.

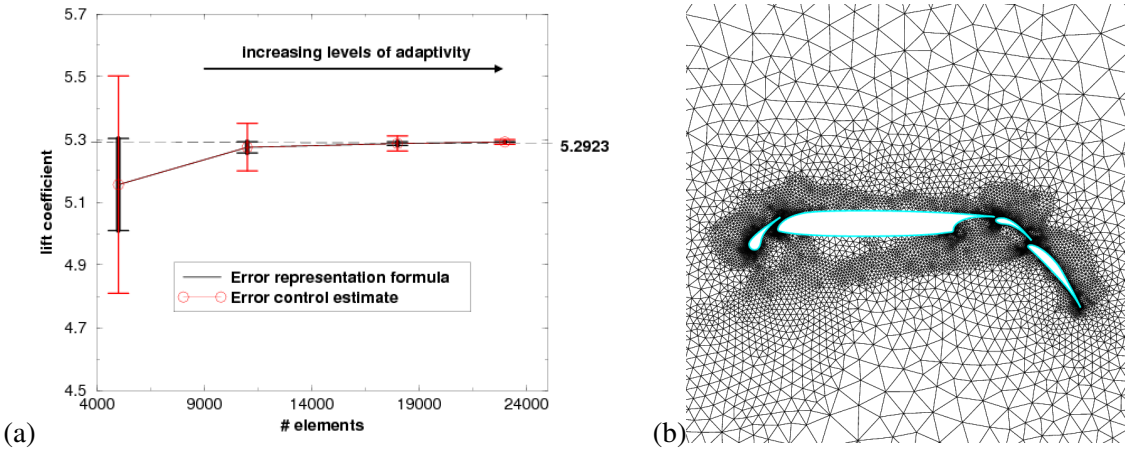

Figure 30. Adaptive mesh refinement for the 5° realization. Shown are (a) graphs of the estimated error in lift coefficient functional using estimates in equations (36) and (37) and (b) the resulting adapted mesh with 18,000 elements after two levels of adaptive refinement.

the adaptive mesh obtained after two levels of refinement is shown in Figure 30(b). Meshes with 11,000 and 18,000 elements were created after 1 and 2 levels of adaptive meshing, respectively. Using the 18,000 element mesh, $L = 5$ Clenshaw-Curtis quadrature yields a lift coefficient mean value of $.52940 \pm .00650$ and standard deviation of $.00704 \pm .000002$. In this calculation, the error representation equation (35) was used to estimate the realization QOI error. Some computational saving can be achieved by reusing the dual problem solution for different realizations but this assumes that the primal problem linearization error can be neglected. One should weigh the cost and complexity of solving a dual problem against the alternative of simply solving the primal problem with a more accurate method and estimating the realization error from it. This latter approach has a certain appeal but if the estimated realization error is found to be too large, lacking a dual prob-

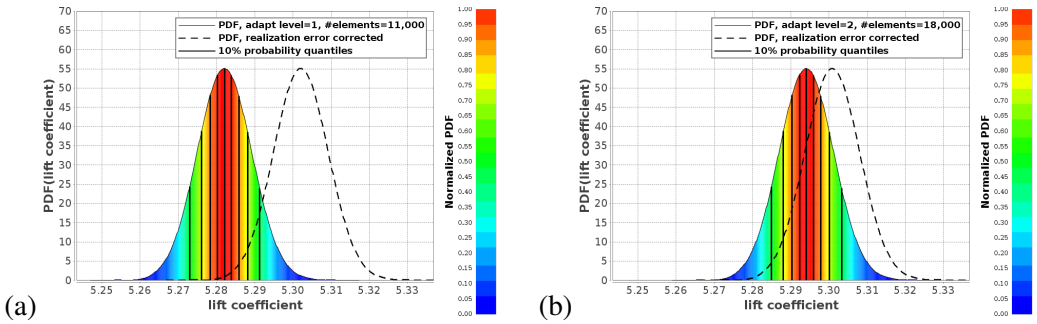

Figure 31. Probability density distributions for the lift coefficient using (a) 11,000 elements and (b) 18,0000 elements for Euler flow over a multi-element airfoil with AOA uncertainty.

lem, the approach does not provide information on how the primal should refined to make the error smaller.

Kernel density estimation in Section 5 has been used to calculate the lift coefficient probability density distribution with and without realization error correction, as shown in Figure 31. Observe in Figure 31 that adding a realization correction does not appear to change the shape, but merely shifts the probability density distribution. This is an expected systematic bias that results from realization error, as discussed in Section 5.3.

6.6 NACA 0012 Airfoil Flow with Correlated Random Field Inflow

Correlated random fields in fluid flow simulations are often introduced to model microscopic spatial or temporal flow perturbations idealized as distributed Wiener processes. A finite correlation between random perturbations at nearby spatial or temporal locations results in a macroscopic scale at which the fluid flow behavior is smooth. A well-known example is the stochastic modeling of a fluid flow in a porous media. A correlated random field is used in these simulations to model the microscale perturbations introduced by the porous material that result in a smooth macroscopic flow field. Random fields also naturally arise in fluid flow simulations as a model of initial and boundary data subject to correlated random perturbations. The next example demonstrates this use in simulating transonic flow over an airfoil with random field inflow data.

6.6.1 Karhunen-Loeve Representation of Correlated Random Fields

The Karhunen-Loeve (K-L) expansion provides an efficient basis for representing correlated random fields. The K-L expansion represents independent Wiener processes at different locations by a single process modulated by a function depending on location. The K-L expansion for a function $f(t,\omega)$ takes the form:

$$f(t,\omega) = \sum_{i=1}^{\infty} \sqrt{\lambda_i}\, \xi_i(\omega)\, \psi_i(t) \tag{56}$$

with $\psi_i(t)$ orthogonal eigenfunctions and λ_i eigenvalues of a correlation function $C(t_1,t_2)$ with spectral representation:

$$C(t_1,t_2) = \sum_{i=1}^{\infty} \lambda_i \psi_i(t_1)\psi_i(t_2) \tag{57}$$

satisfying the Fredholm integral equation of the second kind for $i = 1,2,\ldots,\infty$

$$\int_D C(t_1,t_2)\psi_i(t_1)\,dt_1 = \lambda_i \psi_i(t_2) \tag{58}$$

From orthogonality of the eigenfunctions ψ_i, it immediately follows that:

$$\xi_i(\omega) = \frac{1}{\sqrt{\lambda_i}} \int_D f(t,\omega)\psi_i(t)\,dt \tag{59}$$

For Gaussian processes, the ξ_i are centered, mutually uncorrelated, random variables with unit variance. Consequently, an n-term K-L expansion results in n uncorrelated random variable dimensions.

6.6.2 Airfoil Flow with Random Field Inflow Data

As an example of random field uncertainty, a 2-D transonic Reynolds-averaged Navier-Stokes flow

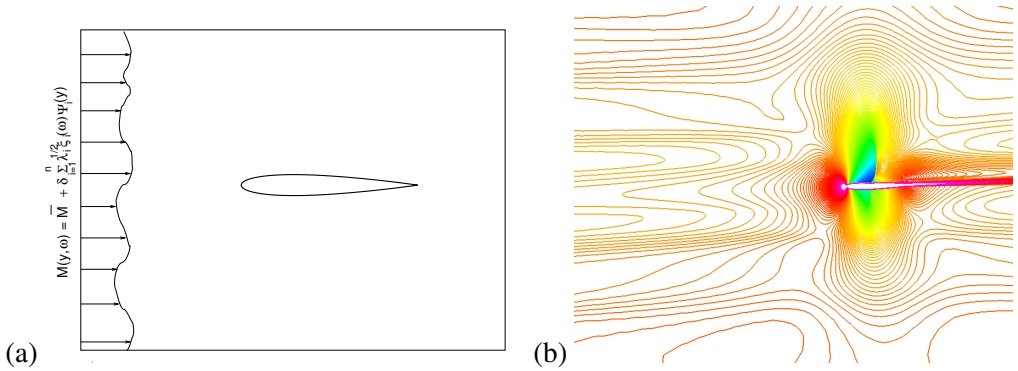

Figure 32. Flow over an airfoil with correlated random field inflow data. Shown are (a) closeup schematic of flow over an airfoil with random field inflow Mach number data, and (b) horizontal velocity component contours for a single Reynolds-averaged Navier-Stokes realization.

field over an airfoil at 2.26° angle-of-attack, with correlated random field inflow data, has been numerically approximated; see the schematic in Figure 32(a) and a sample Reynolds-averaged Navier-Stokes realization in Figure 32(b). The inflow Mach number profile in the vertical dimension y is a random field with exponential correlation:

$$C(y_1,y_2) = \varepsilon^2 e^{-|y_1-y_2|/b} \tag{60}$$

for a specified correlation length b and parameter ε. The associated Fredholm equation (58) using this correlation has a simple analytical solution. This exact solution is readily obtained by twice integrating the Fredholm equation with respect to the independent variable y_2 and applying boundary conditions. Scaled eigenfunctions $\sqrt{\lambda_i}\psi_i(y)$ are graphed in Figure 33(a) for $\sigma = 1.0$, $a = b = 1/2$, and $i = 1,\ldots,10$. For this same problem, the eigenvalues λ_i are graphed in Figure 33(b) for several

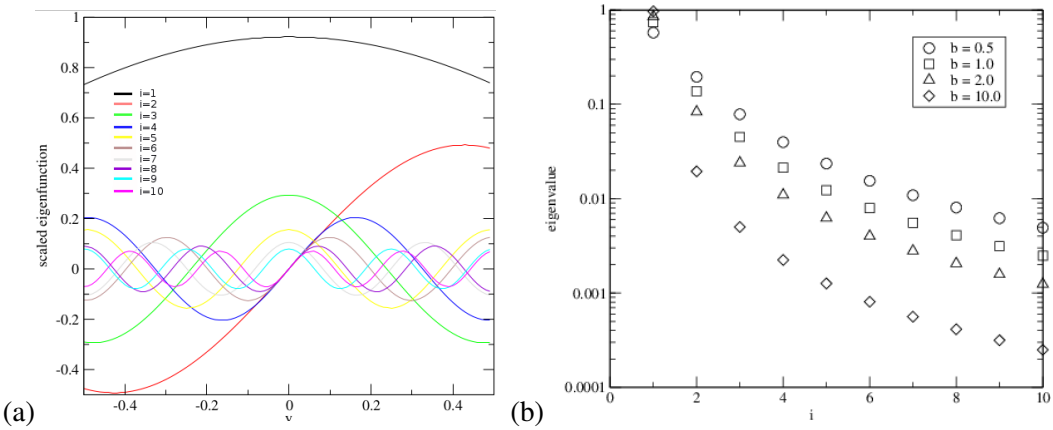

Figure 33. (a) scaled eigenfunctions, $\sqrt{\lambda_i}\psi_i(y)$, for $i = 1,\ldots,10$ and (b) eigenvalues λ_i for correlation lengths $b \in \{0.5, 1.0, 2.0, 10.0\}$.

different correlation lengths b. Observe that the eigenvalues decay rapidly (more so as b increases). This rapid decay motivates the use of the following n-term truncated approximation with mean $\overline{M}$ and scale ε:

$$M(y,\omega) \approx \overline{M} + \varepsilon \sum_{i=1}^{n} \sqrt{\lambda_i}\,\xi_i(\omega)\,\psi_i(y) \tag{61}$$

In the present example, a unit correlation $b = 1$ equal to the airfoil chord length was chosen, $\overline{M} = 0.8$, $\varepsilon = .01$, and the random field approximated by a four-term truncated $K-L$ expansion.

Uncertainty calculations with four random variable dimensions were performed using both sparse and dense tensor product quadratures. Calculations using $L = 4$ sparse Clenshaw-Curtis quadrature required 137 realizations, and calculations using $L = 4$ dense tensor product Clenshaw-Curtis HYGAP approximation required 6,561 CFD evaluations. Figure 34 compares surface pressure coefficient statistics computed using both dense and sparse tensor product quadratures. The sparse tensor product statistics in Figure 34(b) show small oscillations on the lower surface. These spuri-

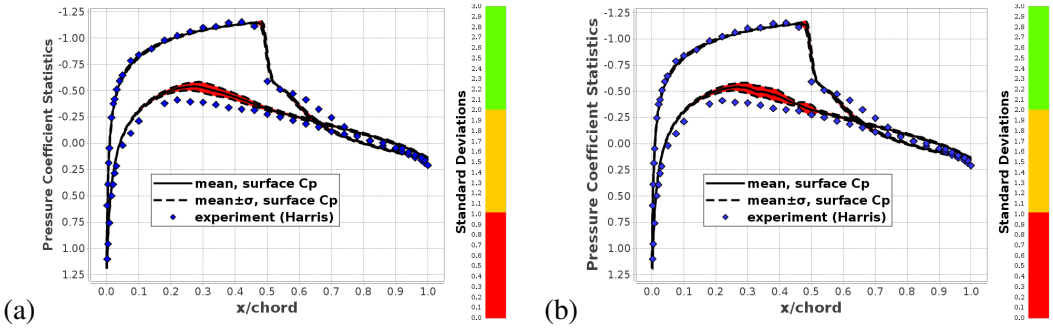

Figure 34. Reynolds-averaged Navier-Stokes flow over a NACA 0012 airfoil with correlated random field inflow data. Shown are surface pressure coefficient mean and standard deviation statistics using (a) $L = 4$ dense tensor product Clenshaw-Curtis HYGAP quadrature and (b) $L = 4$ sparse tensor product Clenshaw-Curtis quadrature.

ous oscillations are due to non-smoothness in the random variable dimensions which significantly

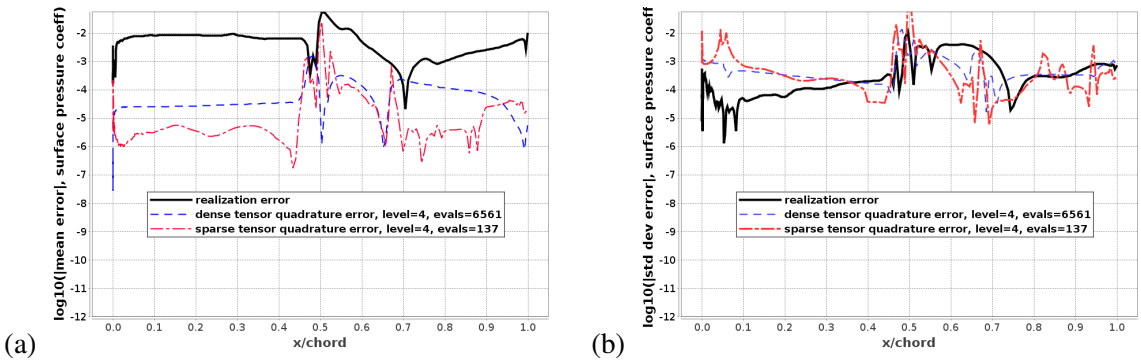

(a) (b)

Figure 35. Navier-Stokes flow over the NACA 0012 airfoil with correlated random field inflow data. Shown are Type I estimates of surface pressure coefficient realization error and sparse/dense quadrature error for (a) mean and (b) standard deviation statistics on the airfoil upper surface.

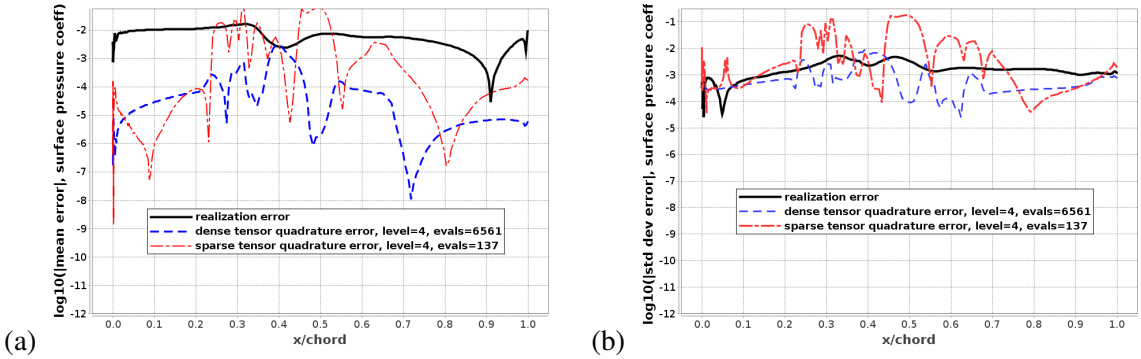

(a) (b)

Figure 36. Navier-Stokes flow over the NACA 0012 airfoil with correlated random field inflow data. Shown are Type I estimates of surface pressure coefficient realization error and sparse/dense quadrature error for (a) mean and (b) standard deviation statistics on the airfoil lower surface.

deteriorates the accuracy of the sparse tensor product quadrature. These spurious oscillations are absent in the Figure 34(a) dense tensor product result because the HYGAP algorithm switches to piecewise polynomial approximation whenever the data becomes non-smooth in random variable dimensions. Examination of the Type I mean and standard deviation error graphs for dense and sparse tensor product quadratures for the upper airfoil surface in Figure 35 and the lower airfoil surface in Figure 36 further confirms the poor accuracy of the sparse tensor product quadrature due to non-smoothness of the underlying statistics integrands. In contrast, the dense Clenshaw-Curtis HYGAP quadrature results shown in figures 35 and 36 show acceptable quadrature error levels, but the computational cost is significantly higher. These calculations show considerable room for improvement in efficiency.

7 Concluding Remarks

Combined uncertainty and error bound estimates provide a quantitative guide when performing practical CFD calculations with uncertainty by:

- Quantifying the overall accuracy of computed output moment statistics.
- Quantifying the impact of statistics integral quadrature error on the accuracy of computed moment statistics.
- Quantifying the impact of realization error on the accuracy of computed moment statistics.
- Providing a systematic procedure for determining whether additional resources should be devoted to solving realizations more accurately (finer grids) or improving the accuracy of computed moment statistics quadratures (more parameter evaluations).

References

1. A. Aitken. On Bernoulli's numerical solution of algebraic equations. *Proc. Soc. Edinburgh*, 46:289–305, 1926.
2. I. Babuska, F. Nobile, and R. Tempone. A stochastic collocation method for elliptic partial differential equations with random input data. *SIAM J. Numer. Anal.*, pages 1005–1034, 2007.
3. B. S. Baldwin and T. J. Barth. A one-equation turbulence transport model for high Reynolds number wall-bounded flows. Technical Report TM-102847, NASA Ames Research Center, Moffett Field, CA, August 1990.
4. T. J. Barth. Numerical methods for gasdynamic systems on unstructured meshes. In Kröner, Ohlberger, and Rohde, editors, *An Introduction to Recent Developments in Theory and Numerics for Conservation Laws*, volume 5 of *Lecture Notes in Computational Science and Engineering*, pages 195–285. Springer-Verlag, Heidelberg, 1998.
5. T. J. Barth. Simplified discontinuous Galerkin methods for systems of conservation laws with convex extension. In Cockburn, Karniadakis, and Shu, editors, *Discontinuous Galerkin Methods*, volume 11 of *Lecture Notes in Computational Science and Engineering*. Springer-Verlag, Heidelberg, 1999.
6. T. J. Barth. A-posteriori error estimation and mesh adaptivity for finite volume and finite element methods. In T. Plewa, T. Linde, and V. Weirs, editors, *Adaptive Mesh Refinement: Theory and Applications*, volume 41 of *Lecture Notes in Computational Science and Engineering*. Springer-Verlag, Heidelberg, 2004.
7. T. J. Barth. On the propagation of statistical model parameter uncertainty in CFD calculations. *Theor. Comput. Dyn.*, 26:435–457, 2012.
8. T. J. Barth. Non-intrusive uncertainty propagation with error bounds for conservation laws containing discontinuities. In *Uncertainty Quantification*, volume 92 of *Lecture Notes in Computational Science and Engineering*, pages 1–55. Springer-Verlag, Heidelberg, 2013.
9. T. J. Barth and M. Larson. A posteriori error estimation for adaptive discontinuous Galerkin approximations of hyperbolic systems. Technical Report NAS-99-010, NASA Ames Research Center, 1999.

10. T. J. Barth and M. Larson. A-posteriori error estimation for higher order Godunov finite volume methods on unstructured meshes. In Herbin and Kröner, editors, *Finite Volumes for Complex Applications III*, pages 41–63. Hermes Science Pub., London, 2002.

11. V. Barthelmann, E. Novak, and K. Ritter. High dimensional polynomial interpolation on sparse grids. *Advances in Computational Mathematics*, 12:273–288, 2000.

12. R. Becker and R. Rannacher. Weighted a posteriori error control in FE methods. In *Proc. ENUMATH-97, Heidelberg*. World Scientific Pub., Singapore, 1998.

13. H. Brass. Error bounds based on approximation theory. In T. Espelid and A. Genz, editors, *Numerical Integration*, pages 147–163. Kluwer Academic Pub, Dordrecht, 1992.

14. C. W. Clenshaw and A. R. Curtis. A method for numerical integration on an automatic computer. *Numer. Math.*, 2:197–205, 1960.

15. B. Cockburn, S. Hou, and C. Shu. TVB Runge-Kutta local projection discontinuous Galerkin finite element method for conservation laws IV: The multidimensional case. *Math. Comp.*, 54:545–581, 1990.

16. B. Cockburn, M. Luskin, C.-W. Shu, and E. Süli. Enhanced accuracy by postprocessing for finite element methods for hyperbolic equations. *Math. Comp.*, 72:577–606, 2003.

17. K. Eriksson, D. Estep, P. Hansbo, and C. Johnson. Introduction to numerical methods for differential equations. *Acta Numerica*, pages 105–158, 1995.

18. T. Gerstner and M. Griebel. Numerical integration using sparse grids. *Numerical Algorithms*, 18(3–4):209–232, 1998.

19. C. Harris. Two-dimensional aerodynamic characteristics of the NACA 0012 airfoil in the Langley 8-foot transonic pressure tunnel. Technical Report TM-81927, NASA Langley Research Center, Hampton, VA, 1981.

20. R. Hartmann and P. Houston. Adaptive discontinuous Galerkin methods for the compressible euler equations. *J. Comp. Phys.*, 182(2):508–532, 2002.

21. D. Jespersen, T. Pulliam, and P. Buning. Recent enhancements to OVERFLOW. Technical Report 97-0644, AIAA, Reno, NV, 1997.

22. G. Jiang and C.-W. Shu. Efficient implementation of weighted ENO schemes. *J. Comp. Phys.*, pages 202–228, 1996.

23. M. Larson and T. Barth. A posteriori error estimation for adaptive discontinuous Galerkin approximations of hyperbolic systems. In Cockburn, Karniadakis, and Shu, editors, *Discontinuous Galerkin Methods*, volume 11 of *Lecture Notes in Computational Science and Engineering*. Springer-Verlag, Heidelberg, 1999.

24. P. LeSaint and P. Raviart. On a finite element method for solving the neutron transport equation. In C. de Boor, editor, *Mathematical Aspects of Finite Elements in Partial Differential Equations*, pages 89–145. Academic Press, 1974.

25. N. Metropolis and S. Ulam. The Monte Carlo method. *J. Amer. Stat. Assoc.*, 44(247):335–341, 1949.

26. H. Niederreiter. Low-discrepancy and low-dispersion sequences. *J. Num. Th.*, 30:51ąV70, 1988.

27. E. Novak and K. Ritter. High dimensional integration of smooth functions over cubes. *Numer. Math.*, 75(1):79–97, 1996.

28. E. Parzen. On estimation of a probability density function and mode. *Annals of Mathematical Statistics*, 33:1065–1076, 1962.

29. T. Patterson. The optimum addition of points to quadrature formulae. *Math. Comp.*, 22:511–520, 1993.

30. S. Prudhomme and J. Oden. On goal-oriented error estimation for elliptic problems: application to the control of pointwise errors. *Comp. Meth. Appl. Mech. and Eng.*, pages 313–331, 1999.

31. W. H. Reed and T. R. Hill. Triangular mesh methods for the neutron transport equation. Technical Report LA-UR-73-479, Los Alamos National Laboratory, Los Alamos, New Mexico, 1973.

32. L. Richardson and J. Gaunt. The deferred approach to the limit. *Trans. Royal Soc. London, Series A*, 226:299–361, 1927.

33. M. Rosenblatt. Remarks on some nonparametric estimates of a density function. *Annals of Mathematical Statistics*, 27:832–837, 1956.

34. V. Schmitt and F. Charpin. Pressure distributions on the ONERA M6 wing at transonic mach numbers. Technical Report AGARD AR-138, Advisory Group for Aerospace Research and Development, 1979.

35. T. Sclafani, J. Slotnick, J. Vassberg, T. Pulliam, and H. Lee. Overflow analysis of the nasa trap wing model from the first high lift prediction workshop. Technical Report 2011-0866, AIAA, Orlando, FL, 2011.

36. J. Slotnick, J. Hannon, and M. Chaffin. Overview of the first aiaa cfd high lift prediction workshop. Technical Report 2011-0862, AIAA, Orlando, FL, 2011.

37. R. Smith. *Uncertainty Quantification*. SIAM Pub, Philadephia, 2014.

38. S. Smolyak. Quadrature and interpolation formulas for tensor products of centain classes of functions. *Dok. Akad. Nauk SSSR*, 4:240–243, 1993.

39. M. A. Tatang. *Direct Incorporation of Uncertainty in Chemical and Environmental Engineering Systems*. PhD thesis, MIT, 1994.

40. B. van Leer. Towards the ultimate conservative difference schemes V. A second order sequel to Godunov's method. *J. Comp. Phys.*, 32:101–136, 1979.

41. B. van Leer. Upwind-difference schemes for aerodynamics problems governed by the Euler equations. volume 22 of *Lectures in Applied Mathematics*. AMS Pub., Providence, Rhode Island, 1985.

42. G. Wasilkowski and H. Woźniakowski. Explicit cost bounds on algorithms for multivariate product problems. *J. Complexity*, 11:1–56, 1995.

43. O. C. Zienkiewicz and J. Z. Zhu. The superconvergent patch recovery and a posteriori error estimates. Part I: the recovery technique. *Int. J. Numer. Meth. Engrg.*, 33:1331–1364, 1992.